

This is an Open Access document downloaded from ORCA, Cardiff University's institutional repository:<https://orca.cardiff.ac.uk/id/eprint/100689/>

This is the author's version of a work that was submitted to / accepted for publication.

Citation for final published version:

Uebbing, B., Forootan, Ehsan , Braakmann-Folgmann, A. and Kusche, J. 2017. Inverting surface soil moisture information from satellite altimetry over arid and semi-arid regions. *Remote Sensing of Environment* 196 , pp. 205-223.
10.1016/j.rse.2017.05.004

Publishers page: <http://dx.doi.org/10.1016/j.rse.2017.05.004>

Please note:

Changes made as a result of publishing processes such as copy-editing, formatting and page numbers may not be reflected in this version. For the definitive version of this publication, please refer to the published source. You are advised to consult the publisher's version if you wish to cite this paper.

This version is being made available in accordance with publisher policies. See <http://orca.cf.ac.uk/policies.html> for usage policies. Copyright and moral rights for publications made available in ORCA are retained by the copyright holders.



29 model) is available. Our ARSSM products are also validated against Soil Moisture and
30 Ocean Salinity (SMOS) L3 products, for which maximum correlation coefficients of big-
31 ger than 0.8 are found. Our results also indicate that ARSSM can validate the simulation
32 of hydrological models at least at seasonal time scales.

33 *Keywords:* Altimetry, Backscatter, Altimetry Reconstructed Soil Moisture, Australia,
34 Inversion

35 **1. Introduction**

36 Soil moisture storage is the main driver of the outgoing hydrological fluxes, such as
37 evapotranspiration and (sub-)surface runoff (Katul et al., 2012), two important compo-
38 nents of the terrestrial water cycle. Therefore, quantifying spatio-temporal variability
39 of soil moisture is essential for modeling and understanding the water cycle, including
40 land-atmosphere interactions, as well as for simulating present day and future climate
41 change, and for flood and drought prediction (see, e.g., Rötzer et al., 2014). Nowadays,
42 soil moisture remote sensing has attracted growing interest to complement the sparse
43 available in-situ networks. The contribution of remote sensing techniques is in particular
44 in monitoring of the top soil layer (first few centimeters).

45 Starting with the C-Band (5 GHz) wind-scatterometers on-board of the European
46 Remote Sensing satellites ERS-1 (launched 1991) and ERS-2 (launched 1995), it was
47 demonstrated that the scatterometer data could be applied to estimate vegetation and
48 soil characteristics over continental land surfaces (Mougin et al., 1995). In fact, the
49 backscattered signal energy is linked to the soil water content via the dielectric con-
50 stant (Ulaby et al., 1982). In 2002, the National Aeronautics and Space Administration
51 (NASA) launched the Aqua satellite mission that carried the Advanced Microwave Scan-
52 ning Radiometer (AMSR-E) to observe (passive-mode) brightness temperatures at six
53 dual polarized frequencies (Njoku et al., 2003). Lower microwave frequencies (e.g. C- or
54 X-Band) allow a better monitoring of the upper few centimeters of the Earth's surface
55 (Njoku et al., 2003) with reduced sensitivity to vegetation cover and surface roughness
56 (Draper et al., 2009). To continue the coverage provided by the ERS missions, the
57 Advanced Scatterometer (ASCAT) was launched in 2006 on-board a Meteorological Op-

58 erational (METOP) satellite (Bartalis et al., 2007).

59 The Soil Moisture and Ocean Salinity (SMOS) satellite, a dedicated soil moisture
60 monitoring mission, was launched in 2009 to provide brightness temperature and soil
61 moisture products on a three-daily basis (Delwart et al., 2008; Montzka et al., 2013).
62 Additionally, the Soil Moisture Active Passive (SMAP) mission (Entekhabi et al., 2010),
63 launched in early 2015, has been monitoring continental soil moisture changes with its
64 passive radiometer and active L-Band scatterometer. However, the active instrument
65 failed after six month of operation. Table 1 provides a short summary on the individual
66 missions.

Table 1: Summary of key features of individual soil moisture missions, as well as altimetry mission utilized in this study. Note that the across-track (act) resolution refers to the maximum distance between the tracks at the equator while the along-track (alt) refers to the distance between individual 20 Hz measurements. For SMAP we only report the spatial resolution of the passive radiometer.

Mission	Launch	Sensor	Temporal Resolution	Spatial Resolution
ERS-1/-2	1991/07	Scatterometer C-Band	3-4 d	50-60 km
Aqua	2002/05	AMSR-E: C-Band	3 d	75x43 km
METOP	2006/10	ASCAT: C-Band	2 d	50 km
SMOS	2009/11	MIRAS: L-Band	3 d	35 km
SMAP	2015/01	L-Band	2-3 d	40 km
Envisat	2002/03	active Ku- and S-Band	35 d	300 m alt, 80 km act
Jason-2	2008/07	active Ku- and C-Band	10 d	300 m alt, 315 km act

67 Dedicated satellite altimetry missions (e.g., Envisat, Topex/Poseidon and its follow-
68 on Jason 1, 2, and 3) have been originally designed to measure sea surface height
69 over the oceans (Shum et al., 1995). Over land, the measured backscatter is closely
70 related to soil characteristics at the satellite nadir (Papa et al., 2003; Blarel et al., 2015).
71 Ridley et al. (1996) and Fatras et al. (2012) found high correlation between in-situ soil
72 moisture measurements and altimetry backscatter from the Topex/Poseidon and Envisat
73 missions. Fatras et al. (2015) extended these investigations to different land cover regions,
74 such as desert, savanna and forests. They compared Jason-2 backscatter with side-
75 looking scatterometers (QuickSCAT and ASCAT) over the arid regions of West Africa and
76 found altimetry results to be more sensitive to soil moisture variations and considerably
77 less to vegetation effects, due to the nadir-looking instrument on-board of the satellite.
78 Ka-Band measurements of the Satellite with Argos and Altika (SARAL) mission were
79 assessed by Frappart et al. (2015) to relate the backscatter estimates to spatio-temporal

80 changes in surface roughness, land cover, and soil moisture changes over West Africa.
81 Their study indicates that Ka-Band measurements are able to penetrate underneath
82 the canopy of tropical forests in non-inundated areas. In Table 2, relevant studies that
83 utilize altimetry for soil moisture studies are summarized. We believe that altimetry
84 missions (1) provide high resolution along-track measurements (~ 300 m) of backscatter
85 with (2) low sensitivity to vegetation in combination with (3) more than two decades
86 of continuous measurements which makes altimetry a valuable and independent tool for
87 measuring surface soil moisture. However, due to the limited (across-track) spatial and
88 temporal resolution (Table 1), the range of applications for altimetry based soil moisture
89 monitoring might be limited and the data should be utilized in combination with the
90 existing dedicated soil moisture missions.

91 Estimating surface soil moisture (SSM) from brightness temperatures as measured by
92 dedicated soil moisture missions, or from backscatter observations as measured by altime-
93 try, is challenging. Several previous studies formulated this conversion based on a linear
94 change detection approach (Wagner et al., 1999) and applied to SMOS observations. For
95 example, Liu et al. (2011) combined active (ASCAT) and passive (AMSR-E) products
96 and rescaled them against the simulation of the Global Land Data Assimilation System
97 (GLDAS, Rodell et al., 2004). In Piles et al. (2011), SMOS products were combined and
98 downscaled to 1 km using high resolution VIS/IR MODIS observations. Al-Yaari et al.
99 (2015) applied a multiple-linear regression approach to minimize the differences between
100 AMSR-E and SMOS soil moisture products. An artificial neural network was used to
101 estimate soil moisture from simulated brightness temperatures as in Liou et al. (2001),
102 Angiuli et al. (2008), and Chai et al. (2010). Recently, Rodríguez-Fernández et al. (2015)
103 applied a neural network to identify the statistical relationship between a reference soil
104 moisture data set and a variety of information from SMOS brightness temperatures, C-
105 Band backscatter coefficients from ASCAT and MODIS derived Normalized Difference
106 Vegetation Index (NDVI) data.

107 Converting altimetry backscatter to soil moisture storage is accompanied with diffi-
108 culties including (i) the noisy behavior of the backscatter estimates as a result of strong
109 reflections from surface water in the radar footprint or variations of surface roughness, (ii)

110 the assumptions, such as homogeneous surface conditions in the radar footprint, and (iii)
 111 the need of interpolation between the altimetry tracks. In this study, we present a novel
 112 approach to retrieve soil moisture from satellite altimetry backscatter measurements.
 113 The main objectives are:

- 114 1. to develop an inversion approach which utilizes spatial patterns of modeled soil
 115 moisture to constrain altimetry backscatter and estimate meaningful surface soil
 116 moisture (SSM) information along the altimeter track (Section 4.2);
- 117 2. to validate the altimetry reconstructed SSM estimates by comparing them with
 118 model simulations and with satellite products (e.g. Section 5.2 and 5.3); and
- 119 3. to explore the behavior of altimetry derived SSM within regions with varying land
 120 cover, soil moisture content and topography (e.g. Section 6.3).

Table 2: Studies that utilize satellite altimetry backscatter in context of examining SSM.

Study	Data used	Location	Key results
Ridley et al. (1996)	Topex Ku- and C-Band, modeled backscatter from surface roughness, soil moisture, vegetation, and topography	Simpson Desert, Australia	<ol style="list-style-type: none"> 1. Soil moisture is found to be the dominant component 2. No significant temporal variation is found due to changes in topography and vegetation cover 3. Effects from precipitation on soil moisture decay after about 2 days
Papa et al. (2003)	Topex Ku- and C-Band and C-minus Ku-Band	global	<ol style="list-style-type: none"> 1. Backscatter is related to soil characteristics 2. Altimetry has the potential to monitor land surfaces at global and regional scales
Fatras et al. (2012)	Envisat Ku- and S-Band, in-situ soil moisture station, ASCAT data	Sahel region, Mali	<ol style="list-style-type: none"> 1. Linear relationship is considered between backscatter and SSM 2. Vegetation influence on SSM from altimetry is small 3. Quality of SSM from altimetry using a change detection approach depends on distance to the in-situ station, presence of open water surfaces, topography, and chosen retracking algorithm.
Fatras et al. (2015)	Jason-2 Ku- and C-Band, Envisat Ku-Band, QuikSCAT and ASCAT scatterometry data	West Africa	<ol style="list-style-type: none"> 1. Nadir-looking altimeters are found to be more sensitive to SSM than side-looking scatterometers 2. Impact of vegetation on altimetry backscatter is low 3. Magnitudes of band-dependent backscatter change over different surface types
Frappart et al. (2015)	Jason-2 Ku- and C-Band, Envisat Ku- and S-Band, Saral/Altika Ka-Band	West Africa	<ol style="list-style-type: none"> 1. Altimeter radar echos at nadir incidence are well correlated to soil moisture in semi-arid areas 2. Altimeters are able to detect the presence of water even under dense canopies at all frequencies 3. Only Ka-Band is found capable of penetrating underneath the canopy of non-inundated tropical forest

This study	Jason-2 Ku- and C-Band, Envisat Ku-Band, SMOS derived SSM, AWRA and GLDAS top level soil moisture model data, and ERA-Interim precipitation	Western Australia, Australia	<ol style="list-style-type: none"> 1. Spatial patterns extracted from model data are used to constrain measured backscatter and to convert to SSM 2. Inversion approach 3. Validation against model data and SMOS derived SSM indicates good agreements within (semi-)arid regions with varying land cover, surface roughness, vegetation coverage and human influence
------------	---	------------------------------	---

121 2. Study Area

122 We select a large part of the semi-arid and arid Western Australia as our study area,
123 which covers about one third of the continent i.e. an area of approximately 2.53 million
124 square kilometers. In contrast to earlier studies (Piles et al., 2011; van der Schalie et al.,
125 2015), no in-situ networks of terrestrial soil moisture stations are available here. In
126 the northwest and central parts, the predominant climate is semi-arid to arid, and in the
127 southwest, a more temperate semi-arid to Mediterranean climate can be found. Top level
128 soil moisture in Western Australia is primarily driven by precipitation suggesting a strong
129 land-atmosphere coupling (Bartalis et al., 2007; Draper et al., 2009). This will provide
130 an opportunity to compare estimated altimetry derived soil moisture patterns with those
131 from a global and a continental land surface model. The central part of Western Australia
132 is relatively dry with sparse vegetation coverage (Donohue et al., 2008; Glenn et al., 2011,
133 Fig. 1 and 2), thus, it makes a good study area to test the proposed framework, although,
134 we do not expect a significant contribution of vegetation cover in the altimetry backscatter
135 (Frappart et al., 2015). Two sub-regions are considered in this study. Region A (area
136 of about 1.47 million square kilometers), is defined by longitudes from $113^{\circ}E$ to $126^{\circ}E$
137 and latitudes between $30^{\circ}S$ and $18^{\circ}S$ in Fig. 1 (left), including the (semi-)arid northern
138 and central part of Western Australia. Region B (area of about 0.37 million square
139 kilometers) is defined within the longitude bounds $114^{\circ}E$ to $122^{\circ}E$ and latitude bounds
140 $35^{\circ}S$ to $30^{\circ}S$ in Fig. 1 (right), and covers the southwest of the continent. General land
141 cover classes within both regions derived from MODIS are shown in Fig. 1. Classification
142 is implemented according to the International Geosphere Biosphere Programme (IGBP)
143 scheme by the ‘AusCover’ facility available from the Terrestrial Ecosystem Research
144 Network (TERN, <http://www.auscover.org.au/>).

145 In region A, the surface is mostly covered by shrublands mixed with grassland and
 146 savanna, especially in the western central part, while in the north and northeast of region
 147 A, the coverage is denser. In region B, pronounced variation in land cover can be found,
 148 ranging from dryer shrubland and savanna regions in the northeast and east to the wetter
 149 southwest area. Agricultural land use can be seen in the central and western parts, as
 150 well as some forest areas in the southwest.

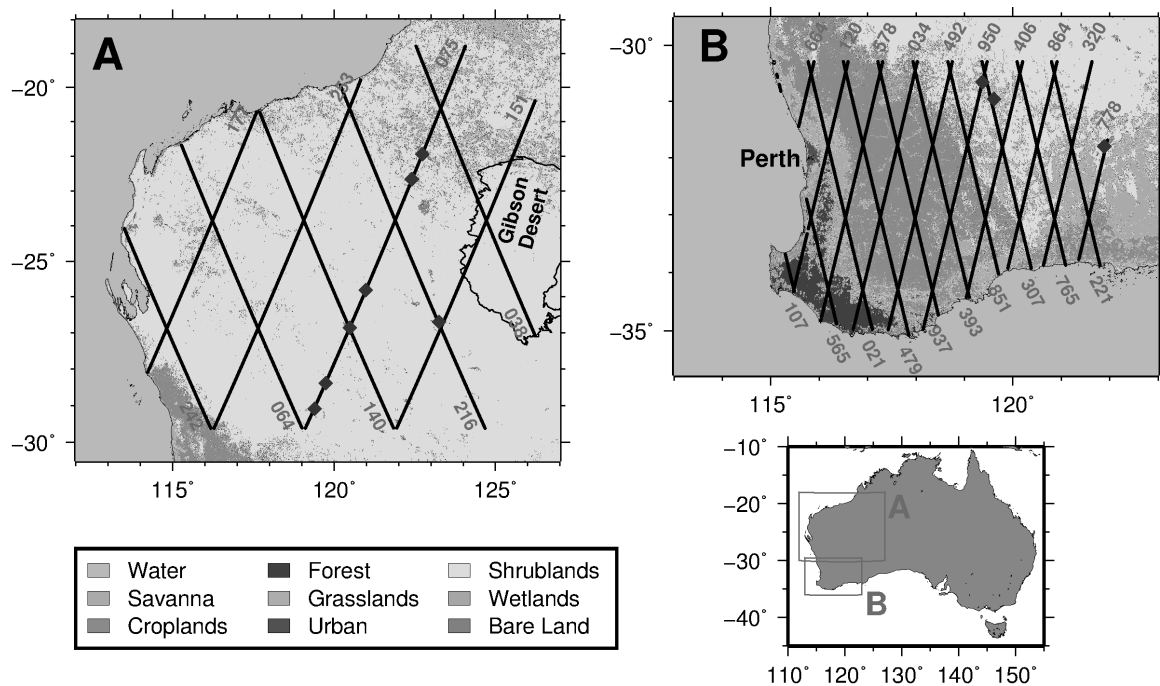


Figure 1: Study areas A and B, where soil moisture information is extracted from satellite altimetry within Western Australia. Land cover classes for the year 2008 are shown. (A) The case study in the northern part of Western Australia used for estimating ARSSM from Jason-2 observations, and (B) includes the southern part of Western Australia utilized for estimating ARSN from Envisat observations. The black lines denote the Jason-2 and Envisat nominal repeat tracks. The corresponding pass numbers are shown close to the tracks. The blue diamonds indicate the locations of surface waters along track 075 (Sec. 4.1, Fig. 2) and the lakes which are explicitly mentioned in the following text.

151 3. Data

152 3.1. Satellite Radar Altimetry Observations

153 Observed waveforms from the Sensor Geophysical Data Records (SGDR) of the Jason-
 154 2 (2008-2014) and European Environmental Satellite (Envisat, 2002-2010) missions are

155 used to derive backscatter (σ_0) information. For both missions the diameter of the pulse
156 limited footprint is between 2-10 km depending on topography over land surfaces (Chelton
157 et al., 2001).

158 **Jason-2:** The Ocean Surface Topography Mission (OSTM) / Jason-2 mission was
159 launched in June, 2008 as a follow-on mission to Jason-1. The satellite orbits the Earth
160 in a near circular \sim 10-day repeat orbit at an altitude of approximately 1336 km with an
161 inclination of 66 deg and a groundtrack separation of about 315 km at the equator. The in-
162 struments on board of the satellite include the altimeter, a radiometer for deriving wet tro-
163 posphere corrections, as well as GPS and DORIS systems for precise orbit determination
164 (Desjonquères et al., 2010). The Poseidon-3 altimeter on board Jason-2 emits radar pulses
165 at Ku-Band (13.575 GHz/2.21 cm) and C-Band (5.3 GHz/5.08 cm) to derive ionospheric
166 electron content influencing the radar signal (Desjonquères et al., 2010; AVISO, 2015).
167 Jason-2 SGDR data include the 20 Hz positions, Ku- and C-Band waveforms, correspond-
168 ing scaling factors, and automatic gain control (AGC) information, as well as 1 Hz atmo-
169 spheric backscatter attenuation corrections and quality flags. However, the flags may not
170 be fully reliable over land influenced regions (Birkett & Beckley, 2010). The Jason-2 data
171 have been acquired from the CNES Archiving, Validation and Interpretation of Satel-
172 lite Oceanographic (AVISO) team (<ftp://avisoftp.cnes.fr/AVISO/pub/jason-2/>).
173 Backscatter information within region A is estimated by reprocessing Jason-2 waveforms
174 between mid of 2008 and end of 2014 according to section 4.1. The nine Jason-2 tracks
175 with their identification numbers are displayed in Fig. 1 (A).

176 **Envisat:** The Envisat satellite was launched in March, 2002 as a follow-on mission
177 to ESA's ERS-1 and ERS-2 missions. The satellite flies on a \sim 35-day sun-synchronous
178 repeat orbit with an altitude of 800 km and inclination of 98.55 deg. This results in
179 a groundtrack separation of approximately 80 km at the equator. Among the 10 in-
180 struments on the satellite, a microwave radiometer that allows estimating the liquid
181 water content of the atmosphere, and the DORIS positioning system and retro reflec-
182 tors for ground bases satellite laser ranging (SLR) enable precise orbit determination
183 (Zelli, 1999). The Radar Altimeter 2 (RA2) altimetry instrument operates in Ku-Band
184 (13.575 GHz/2.2 cm) and S-Band (3.2 GHz/9.37 cm) (ESA, 2007). However, on January

185 18, 2008 the S-Band transmission power dropped significantly, rendering all S-Band obser-
186 vation from this date onward unfeasible. Envisat observations (2002-2010) are examined
187 over the region B in Fig. 1 (B). The distances between Envisat repeat tracks are smaller
188 than those of Jason-2. The Envisat RA2 data was provided to this study by the European
189 Space Agency (ESA, <https://earth.esa.int/>).

190 *3.2. Land Surface Model Data*

191 A-priori soil moisture data is required to derive EOFs within the proposed inversion
192 (see section 4.2). In this study, we use top layer soil moisture from the Global Land
193 Data Assimilation System (GLDAS) (Rodell et al., 2004) and from the Australian Water
194 Resources Assessment (AWRA) system (Vaze et al., 2013).

195 **GLDAS:** We use 3-hourly GLDAS-2.1 land surface model data produced by NOAA
196 and available through the Goddard Earth Sciences Data and Information Services Center
197 (<http://disc.sci.gsfc.nasa.gov/services/grads-gds/gldas>) with a resolution of 1
198 degree. The soil moisture is provided in 4 layers (0-10 cm, 10-40 cm, 40-100 cm and 100-
199 200 cm) in units of kg/m². In this study, we utilize the water storage of the first layer
200 since the altimeter backscatter derived from Ku- and C-Band (or S-Band) frequencies is
201 only sensitive to the first few centimeters of the soil water content.

202 **AWRA:** The AWRA Landscape model (AWRA-L) simulates evapotranspiration,
203 runoff, and soil moisture for the Australian continent on a 0.05 deg (~5.5 km) grid.
204 AWRA employs two hydrological response units (HRU) corresponding to different veg-
205 etation root depths. Before combining the two flux and storage outputs, the HRUs are
206 modeled separately, e.g., considering varying access to individual soil layers. The soil
207 moisture information is subdivided into upper (0-10 cm), lower (10-100 cm) and deep
208 (100-600 cm) layers. For this study, we used daily top-layer soil moisture provided by
209 the Commonwealth Scientific and Industrial Research Organization (CSIRO). The soil
210 moisture values are scaled between 0 and 1 in units of m³/m³, with a maximum capacity
211 value for top-layer water storage of 3 cm, which means that the model values are capped
212 at 0.3 m³/m³.

213 3.3. ERA-Interim Precipitation Reanalysis

214 ERA-Interim precipitation reanalysis data (Dee et al., 2011) is available from the
215 European Centre for Medium-Range Weather Forecasts (ECMWF). The data product is
216 available from <http://www.ecmwf.int/>. In this study, we utilize global grids with 0.75°
217 resolution of total precipitation in meters from 2002 to 2014 which are available every
218 twelve hours at 12 p.m. and 12 a.m., respectively. The data have been accumulated
219 for the last 3-days before the altimeter crossing the study area in order to validate the
220 altimeters' ability to detect past rainfall events of several days before (Ridley et al., 1996).

221 3.4. Soil Moisture and Ocean Salinity (SMOS) Products

222 Daily level-3 products from the ESA-satellite SMOS are available from [http://](http://cp34-bec.cmima.csic.es/land-datasets/)
223 cp34-bec.cmima.csic.es/land-datasets/, based on the level-2 soil moisture User
224 Data Product (UDP) (SMOS-BEC, 2015). The SMOS satellite covers the total sur-
225 face of the Earth every three days. The daily grids with a resolution over Australia of
226 about 0.25° include only the last overflight within each three days and the data product
227 is divided into ascending and descending tracks, with the ascending data referring to
228 approximately 6 a.m. and the descending data referring to approximately 6 p.m. local
229 time. The soil moisture information is provided in terms of percentage, between 0 and
230 1 (ESA, 2014). Soil moisture values derived from SMOS L3 ('SMOS' from now on) over
231 Western Australia are found mostly in the range of 0 to 0.5, where 0.5 corresponds to
232 $0.5m^3$ of water per $1m^3$ of soil.

233 4. Methods

234 Backscatter nadir measurements at a rate of 20 Hz (every ~ 300 m along-track) of
235 Jason-2 (Ku- and C-Band) and Envisat (Ku- and S-Band) altimetry missions, that pro-
236 vide new measurements every ~ 10 days (Jason-2, 2008 - 2014) or ~ 35 days (Envisat,
237 2002 - 2010), are examined over the arid and semi-arid Western Australia.

238 The proposed inversion approach consists of four steps: (i) along-track backscatter
239 are estimated by post-processing the altimetry waveforms as described in section 4.1. (ii)

240 Principal Component Analysis (PCA, Preisendorfer, 1988) is applied to extract the dom-
 241 inant orthogonal modes of top level soil moisture storage simulated by either a global or
 242 regional hydrological model along the altimetry tracks in (i). (iii) We employ all available
 243 spatial empirical orthogonal functions (EOFs) of (ii), and use them in an inversion pro-
 244 cedure as a-priori information (base-functions) for fitting to the backscatter observations
 245 of (i). (iv) The results of step (iii) are the altimetry derived temporal variability that
 246 are used to derive altimeter reconstructed surface soil moisture (ARSSM) products that
 247 represent the top soil level storage changes (see section 4.2 for details).

248 Our results suggest that the proposed method works well in different regions. Here,
 249 we validate the results in a (semi-)arid region because this allows us to neglect influences
 250 on the backscatter measurement, e.g. seasonal variations in snow cover, which otherwise
 251 would have to be removed from observations. For validation, we compare our recon-
 252 structed SSM to reanalysis precipitation data from ERA-Interim (Dee et al., 2011). Our
 253 assumption is that rainfall is the main driver of soil moisture in the semi-arid regions, as
 254 well as to top level soil moisture extracted from global and regional models. Furthermore,
 255 we assess the differences with respect to SMOS L3 soil moisture (SMOS-BEC, 2015).

256 4.1. Processing Altimeter Waveforms

257 Backscatter (σ_0) can be estimated by post-processing altimetry waveforms as (ESA,
 258 2007)

$$\sigma_0 = s + q + \Delta_{atm}, \quad (1)$$

259 with

$$q = 10 \log_{10}(Pu), \quad (2)$$

260 where q is the term derived from retracking the altimeter return waveform and converting
 261 the estimated amplitude Pu to decibel using equation (2). In equation (1), Δ_{atm} is the
 262 atmospheric attenuation of the backscatter, provided in the SGDR data, and s is the
 263 scaling factor that is derived from the radar equation applied to satellite altimetry (Roca
 264 et al., 2002). The scaling factor is computed by the Envisat and Jason-2 processing
 265 centers and provided in the SGDR data.

266 The shape of the altimeter return waveform over land surfaces usually does not cor-
 267 respond well to known model shapes from open water surfaces, such as the Brown model
 268 (Brown, 1977). Off-nadir surface waters, such as lakes or rivers, introduce peaks into the
 269 waveform, which will significantly influence the geophysical parameters, especially the
 270 amplitude Pu that is computed following Deng et al. (2002)

$$Pu = \sqrt{\frac{\sum_{i=1}^N P_i^4(t)}{\sum_{i=1}^N P_i^2(t)}}, \quad (3)$$

271 with the number of range gates N , and P_i being the return power at the i 'th range gate.
 272 Combining equations (1), (2) and (3) will result in backscatter estimates very similar
 273 to the Off Center Of Gravity (OCOg) or threshold methods, such as ICE-1 which is
 274 included in the GDR data. To suppress the energy from individual off-nadir peaks,
 275 related to surface waters inside the altimeter footprint, we convert the total waveform to
 276 decibel using equation (4)

$$\tilde{P}_i = 10 \log_{10}(P_i). \quad (4)$$

277 We replace P_i in equation (3) with estimated \tilde{P}_i from equation (4) to compute modified
 278 amplitudes $\tilde{P}u$ whose unit is decibel and can replace q in equation (1) to estimate modified
 279 backscatter. The original backscatter (from equations (1), (2), and (3)) shows relatively
 280 larger along-track variations compared to our modified approach, which is considerably
 281 less affected by small peaks on the waveform's trailing edge which we ascribe to small
 282 off-nadir surface waters. In Fig. 2, we correlate the original and modified along-track
 283 backscatter values from Jason-2 with the top level soil moisture information from the
 284 AWRA model. The results indicate higher correlation between the smoother backscatter
 285 estimations $\tilde{\sigma}_0$ from the modified approach with AWRA compared to the backscatter
 286 results (σ_0) from the original approach. Large peaks appear in Fig. 2 (gray regions),
 287 which are related to the strong reflection from surface water. These include Lakes Barlee,
 288 Noondie, Way, Teague, and Dora, as well as the Rundall River, which are also marked
 289 in Fig. 1.

290 The magnitude of the backscatter value is mainly defined by the scaling factor and the

291 corresponding automatic gain control (AGC) value, while the 2nd term in equation (1)
 292 only slightly changes the final results. As a result, the backscatter value (σ^0 derived from
 293 equation (1)) still peaks when the altimeter nadir is close to surface waters. In order
 294 to reduce the influence from surface waters, we compute the difference of along-track
 295 backscatter measurements from consecutive altimetry cycles. This reduces the influence
 296 of slowly varying surface features such as surface roughness, and to some extent, dynamic
 297 changes, e.g., vegetation growth. Therefore, backscatter anomalies (instead of absolute
 298 backscatter) are used to compute soil moisture anomalies.

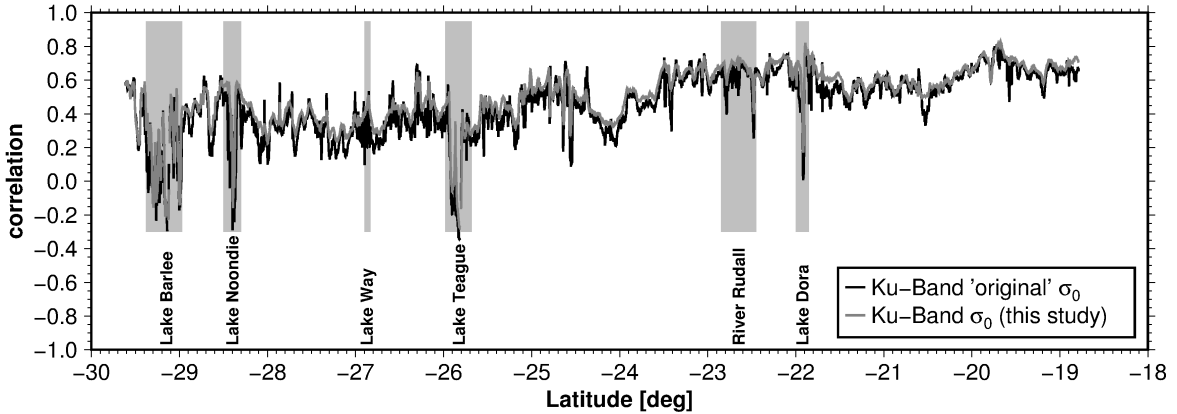


Figure 2: Correlation coefficients between Ku-Band backscatter (σ_0) with AWRA model data along the pass 075 of Jason-2. Two correlation coefficient curves are shown, for σ_0 processed by the original method (black curve, derived from equations (1), (2) and (3)), and the orange curve represents the modified approach. We found similar correlation results from the C-Band backscatter estimations.

299 4.2. An Inversion Framework for Converting Backscatter to Soil Moisture Storage

300 Spatio-temporal variability of altimetry backscatter (denoted by the subscript B) and
 301 of soil moisture storage (denoted by the subscript S) can be arranged in a data matrix
 302 $\mathbf{X}_{B/S}(t, j)$, with t representing the time of observations and j standing for their positions.
 303 We assume that the time series are already centered, i.e. their temporal mean has already
 304 been reduced. The data matrix can be decomposed by Singular Value Decomposition
 305 (SVD, Preisendorfer, 1988) as

$$\mathbf{X}_{B/S}(t, j) = \bar{\mathbf{P}}_{B/S}(t) \mathbf{\Lambda}_{B/S} \bar{\mathbf{E}}_{B/S}^T(j), \quad (5)$$

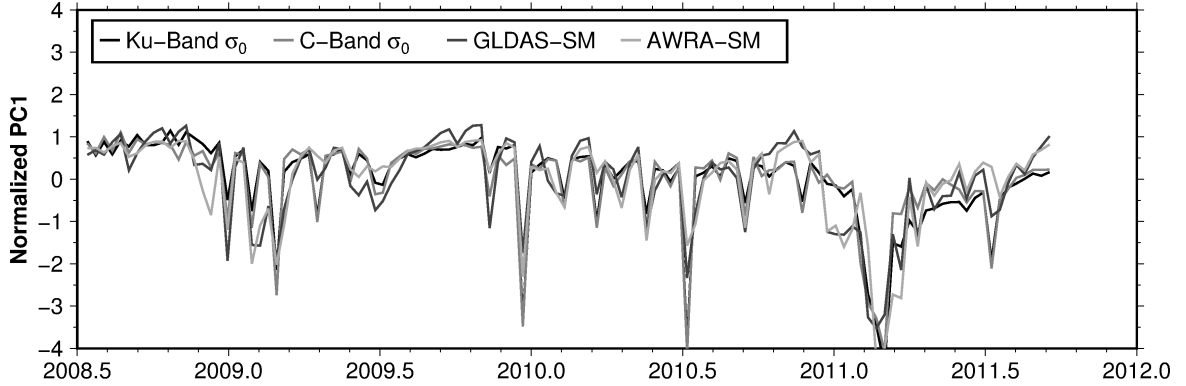


Figure 3: Normalized first principal component (PC) derived by applying equation (5) to along-track altimetry backscatter (σ_0 data from Ku- (35.1%) and C-Band (40.3%)), as well as top level soil moisture simulations of GLDAS (65.6%) and AWRA (44.5%). The PCs are computed along the track 075 of Jason-2 in the northern study area (Fig. 1, region A). All principal components are normalized by their standard deviation. The percentage values in parenthesis provide the amount of total variance explained by the corresponding first PCs.

306 where $\bar{\mathbf{P}}_{B/S}(t)$ contains normalized temporal principal components (PCs), $\mathbf{\Lambda}_{B/S}$ is a di-
307 agonal matrix that holds the singular values λ ordered according to their magnitude,
308 and $\bar{\mathbf{E}}_{B/S}(j)$ contains the spatial empirical orthogonal functions (EOFs). PCA allows
309 to extract a large amount of variance (of $\mathbf{X}_{B/S}$) in relatively few orthogonal modes.
310 PCs ($\bar{\mathbf{P}}_{B/S}(t)$) and EOFs ($\bar{\mathbf{E}}_{B/S}(j)$) in equation (5) are unit-less and orthogonal, i.e.
311 $\bar{\mathbf{P}}_{B/S}^T(t)\bar{\mathbf{P}}_{B/S}(t) = \mathbf{I}$ and $\bar{\mathbf{E}}_{B/S}^T(j)\bar{\mathbf{E}}_{B/S}(j) = \mathbf{I}$ with \mathbf{I} being the identity matrix. We use
312 them as base-functions for comparing altimetry backscatter estimations and model de-
313 rived soil moisture storage or combining them. The standard deviation of variability in
314 the data matrix $\mathbf{X}_{B/S}$ and the measurement unit is reflected in $\mathbf{\Lambda}_{B/S}$, which can be used
315 to relate anomalies of altimetry backscatter to SSM changes.

316 To investigate whether there is a connection between backscatter and soil moisture, we
317 apply equation (5) to the altimetry derived backscatter $\tilde{\sigma}_0$ from along-track Jason-2, Ku-
318 and C-Band (Fig. 3), as well as the top level soil moisture from the GLDAS and AWRA
319 models along the same track. Here, only the temporal evolution of the first dominant
320 PC is shown, for which we find a correlation coefficient of about 0.8 between altimetry
321 backscatter and AWRA/GLDAS derived soil moisture simulations. This provides us
322 with confidence that altimetry backscatter mainly reflect soil moisture variations. The
323 resulting EOFs from GLDAS and AWRA generally agree with the EOFs from GLDAS

324 but show a smoother profile along the track due to the lower spatial resolution of the
 325 GLDAS model data.

326 Considering equation (5), if the altimetry backscatter estimations were linearly related
 327 to the soil storage changes, one could conclude that $\bar{\mathbf{P}}_B$ and $\bar{\mathbf{E}}_B$ are also linearly related
 328 to $\bar{\mathbf{P}}_S$ and $\bar{\mathbf{E}}_S$, respectively. This is however not true considering the relationship in
 329 equations (1) to (4), and due to the differences between noise distribution of backscatter
 330 and soil moisture storage simulations. Therefore, we propose an inversion method to
 331 convert backscatter to soil moisture storage estimations. This can be realized by fitting
 332 the EOFs of the model derived soil storage ($\bar{\mathbf{E}}_S$) to the altimetry backscatter estimations
 333 (\mathbf{X}_B) as

$$\hat{\mathbf{P}}(t) = \mathbf{\Lambda}_B^{-1} [\bar{\mathbf{E}}_S^T(j) \bar{\mathbf{E}}_S(j)]^{-1} \bar{\mathbf{E}}_S^T(j) \mathbf{X}_B(t, j). \quad (6)$$

334 In this estimation, we rely on the spatial distribution of soil moisture storage from a
 335 model. Therefore, $\bar{\mathbf{E}}_S$ are chosen as base-functions that remain invariant within the
 336 inversion. The term $\mathbf{\Lambda}_B^{-1}$ makes the backscatter estimations unit-less. After solving
 337 equation (6), updated temporal patterns ($\hat{\mathbf{P}}$) are estimated that indicate the contribu-
 338 tion of soil moisture storage changes in the backscatter estimations. Finally, altimetry
 339 backscatter are converted to soil moisture storage variability by a PCA reconstruction as

$$\hat{\mathbf{X}}_S(t, j) = \hat{\mathbf{P}}(t) \mathbf{\Lambda}_S \bar{\mathbf{E}}_S^T(j). \quad (7)$$

$$\hat{\mathbf{X}}_{sm}(t, s) = \hat{\mathbf{P}}(t) \mathbf{\Lambda}_{sm} \bar{\mathbf{E}}_{sm}^T(s) \quad (8)$$

$$\hat{\mathbf{P}}(t) = \mathbf{\Lambda}_{\sigma_0}^{-1} [\bar{\mathbf{E}}_{sm}^T(s) \bar{\mathbf{E}}_{sm}(s)]^{-1} \bar{\mathbf{E}}_{sm}^T(s) \sigma_0(t, s) \quad (9)$$

$$\mathbf{X}(t, s) = \bar{\mathbf{P}}(t) \mathbf{\Lambda} \bar{\mathbf{E}}^T(s) \quad (10)$$

5. Results

In the following, the results of estimated altimetry reconstructed surface soil moisture (ARSSM, equation (7)) are presented and compared to model simulations and to independent SSM measurements from SMOS. The model simulations and gridded SMOS data are spatially interpolated to the position of the altimetry tracks. Temporally, we also interpolated the data according to the times when the altimeter crosses the study sites. We then compute differences between backscatter from successive altimetry cycles in order to reduce the signal from constant and slowly changing influences, such as surface roughness or vegetation. For consistency, the same differences are applied to the interpolated model and SMOS data, i.e. we estimate anomalies for each data set along the altimetry tracks. To implement the proposed inversion, we apply PCA to GLDAS and AWRA data, resulting in 34 and 117 EOFs, respectively. For both models, we keep the EOFs that correspond to at least 99% of the variance, i.e. 20 EOFs for GLDAS and 25 for AWRA.

First, the consistency of our ARSSM is examined by computing annual amplitudes and phases and comparing to amplitudes and phases derived from GLDAS and AWRA. Afterwards, along-track comparisons are presented before the investigation is extended to all Jason-2 groundtracks located inside the study region A, and all Envisat groundtracks within the study region B (Fig. 1). Finally, we will examine the differences between soil moisture model simulations and ARSSM estimates. To better visualize the surface topography impact on the estimated ARSSM (e.g., Fig. 4), we use elevation information derived from the SRTM30plus V11 data set (http://topex.ucsd.edu/www_html/srtm30_plus.html). Spatial anomalies of topography changes, derived from subtracting the topography smoothed by a 100km Gaussian filter, are also shown as gray shaded background that likely represent the geometrical roughness. In our study sites, land elevation and spatial anomaly rarely exceed 1000m and 100m, respectively.

5.1. Assessing the Level of Agreement between the ARSSM and Model Simulation/ SMOS

To assess the consistency of the ARSSM, we have computed the annual amplitudes and phases from our inversion results, as well as from the GLDAS and AWRA model data

369 (Fig. 4). Generally we find relatively small amplitudes in the range of ~ 0 to $0.01 m^3/m^3$
370 which vary along the individual tracks with higher amplitudes closer to the coast in the
371 North, as well as over the agricultural areas in the South-West. For the phase component
372 we find similar transition of about 300 days in the South-West to about 60 days in the
373 North-East for ARSSM and the two model data sets. Over the Gibson Desert (Fig. 1,
374 (A)), zero amplitudes from ARSSM (Fig. 4, (A)) and the AWRA model (Fig. 4, (E))
375 are detected, while significant signal is found from the GLDAS model (Fig. 4, (C)).
376 In the central and southern central parts of our study region, the magnitude of the
377 amplitudes from ARSSM (Fig. 4, (A)) tend to agree better with the ones from GLDAS
378 (Fig. 4, (C)) compared to the amplitudes from AWRA (Fig. 4, (E)). We do not find any
379 patterns coinciding with dominant topographic features shown in the background of the
380 sub-figures. The GLDAS phases (Fig. 4, (D)) show less spatial variation compared to
381 the AWRA and ARSSM phases.

382 In Fig. 5 (A) and (B), we directly compare ARSSM anomalies, derived using EOFs
383 from AWRA, with surface soil moisture anomalies from AWRA (A) and SMOS (B) during
384 one arbitrarily chosen date, January 31, 2010, when the Jason-2 satellite was crossing the
385 study site A. The track is outlined by a black polygon and the colors inside represent the
386 ARSSM anomalies. The spatial features of AWRA and SMOS generally agree as both,
387 provide negative anomalies in the north and strong positive anomalies in the central
388 parts. However, although we utilized EOFs from AWRA to derive the ARSSM, Fig. 5
389 (A) shows only weak agreement between AWRA model data and ARSSM on the chosen
390 date. In contrast, ARSSM generally agrees well with the SMOS product in the southern
391 and central parts of the track. In the north, we detect weaker anomalies compared to
392 SMOS (Fig. 5, (B)).

393 *5.2. Along-Track Behavior of the ARSSM*

394 The results of this section refer to the pass 075 of Jason-2 (within region A of Fig.
395 1). Between the latitude of $30^\circ S$ to $24^\circ S$, the land cover is mainly shrublands, while in
396 the north (between $24^\circ S$ and $18^\circ S$), it changes to a mix of shrublands, grasslands and
397 savanna. Four sets of ARSSM products are estimated from either Ku- and C-Band while

398 using the EOFs of GLDAS or AWRA in the inversion (equation (6)). A strong agreement
399 is found between GLDAS and AWRA simulations along the pass 075 of Jason-2, whereas
400 both products are highly correlated (correlation coefficients of 0.6 to 0.8) as shown in
401 Fig. 6. For brevity, we show the ARSSM results based on AWRA EOFs in Fig. 6.

402 Correlation between ARSSM (from Ku- and C-Band) with AWRA is slightly lower
403 than between GLDAS and AWRA, but the ARSSM results suggest a similar quality
404 compared to the SMOS product in the southern part of the track, while ARSSM provides
405 higher correlation coefficients than SMOS in the north. Unlike the correlation coefficients
406 between altimetry backscatter and AWRA (Fig. 2), the ARSSM results do not exhibit
407 large peaks close to the larger surface waters. Our results indicate that soil moisture
408 retrieved from the ascending orbit of SMOS (dashed cyan line) is better correlated with
409 AWRA simulations compared to those derived from the descending orbit (solid cyan
410 line). Additionally, Fig. 6 shows the correlation with respect to the difference of ARSSM
411 estimated from C- minus Ku-Band observations (blue line), which suggest considerably
412 less similarity with model simulations. Therefore, they will no longer be discussed in this
413 paper.

414 Considering the magnitude of correlation coefficients along the altimeter track in Fig.
415 6, in the south (up to a latitude of $\sim 24^\circ S$), one can see smaller values (around 0.4)
416 between ARSSM, as well as SMOS soil moisture and AWRA simulations. To the north,
417 correlation coefficients between ARSSM and AWRA rise to around 0.6 with some points
418 being bigger than 0.7, while those of SMOS do not increase significantly. This behavior
419 coincides roughly with the change of land cover classes from shrublands only in the south
420 to a mixture of shrublands, grasslands and savanna in the north part of Fig. 1 (A).
421 Additionally, the topography in the north is less mountainous, which results in more
422 reliable backscatter measurements and consequently ARSSM estimation.

423 To understand the short-term impact of precipitation on the surface soil moisture vari-
424 ability in this region, we compare model simulations, SMOS, and our ARSSM with 3-day
425 accumulated precipitation anomalies derived from the ERA-Interim reanalysis product
426 (Fig. 7). Generally, the correlation coefficients between ARSSM (from both Ku- and
427 C-Band observations) and precipitation are larger compared to those between precipita-

428 tion and the GLDAS or AWRA model simulations. The top level soil moisture from the
429 GLDAS model shows a rather stable correlation coefficients of about 0.4 in the South,
430 which raises to 0.6-0.7 in the northern part of pass 075 (Fig 7). Top level soil moisture
431 from the AWRA model shows weak correlations (< 0.2) in the south and stronger cor-
432 relation coefficients (0.5 - 0.6) in the northern part of the pass. The correlations with
433 SMOS products for the time period considered here, show a less reliable behavior with
434 rapidly varying correlation coefficients along the track and become negative in the North.

435 *5.3. Surface Soil Moisture Anomalies within Western Australia*

436 We examine the quality of ARSSM estimations over the entire study regions A and
437 B (Fig. 1). Since the ARSSM results from the C- and Ku-Band of Jason-2 are found to
438 be very similar (compare Fig. 6 and 7), we limit the results to the C-Band covering the
439 period 2008-2014. Generally, C-Band is considered to be more sensitive to surface soil
440 moisture due to the longer wavelength which enables better penetration of the surface.
441 The Ku-Band results are summarized in Table 3 and 4. For Envisat, we limit the dis-
442 cussion to the Ku-Band data (2002-2010) since the time series of the S-Band backscatter
443 data is much shorter due to an instrument failure. Consequently, they are not included
444 in Tables 5 and 6, either.

445 *5.3.1. Soil Moisture within Northwestern Australia (Study Region A)*

446 In Fig. 8 (A) and (B), correlation coefficients between the C-Band backscatter and
447 GLDAS as well as AWRA simulations are shown. The magnitude of the correlation
448 coefficients is found to be small < 0.2 at some locations along the track. Generally
449 smaller correlations are found between altimetry backscatter and AWRA simulations
450 (Fig. 8, (B)) compared to those of GLDAS (Fig. 8, (B)). Similar to the results in
451 Fig. 2, these sudden drops in correlation are mainly detected over regions, where the
452 altimetry footprint contains surface water, e.g., passing over lakes and rivers. This can
453 for example be observed at the crossing point of Jason-2 tracks 151 and 216 (see Fig. 1
454 (A) approximately at $123.25^{\circ}E$ and $26.70^{\circ}S$) over Lake Wells (Fig. 1, (A)), where the
455 return signal includes almost no information related to land surface features.

456 EOFs are computed from AWRA simulations and used in equation 6 to invert AR-
457 SSM. These estimations are then correlated with GLDAS and AWRA model simulations
458 (see Fig. 8 (C) and (D)). Another set of ARSSM is also estimated using GLDAS EOFs,
459 and the correlation with model simulations is shown in Fig. 8 (E) and (F). The ARSSM
460 results indicate higher correlation with model simulations (compare Fig. 8 (A) and (B)
461 to the rest).

462 Correlation between ARSSM and model simulations is found to be stronger close to
463 the coast in the west and southwest of the study region A. In the central and southern
464 central parts, ARSSM indicates weak to medium correlation with AWRA, and signifi-
465 cantly stronger correspondence with GLDAS. In the northwest (along the pass 177 in
466 Fig. 1 (A)) very low correlation coefficients are found in Fig. 8 (C) and (D). We ascribe
467 this to significant topography changes along the altimetry ground track. In the eastern
468 part of region A, along the pass 151 of Jason-2 and from the crossing point with the pass
469 38 and north of it, a rather large area with very low correlations can be observed. Surface
470 soil moisture simulations from AWRA do not show any variations over the Gibson Desert
471 (Fig 1) during 2008-2011. As a result, low correlations are derived in this region when
472 either EOFs from AWRA are employed (Fig. 8, (C)) or correlations with respect to the
473 AWRA model data are estimated (Fig. 8 (D) and (F)). In contrast, ARSSM based on
474 GLDAS EOFs is close to GLDAS SSM (Fig. 8, (E)) over the Gibson Desert. This effect
475 is well reflected in Table 3 while comparing the minimum correlations with the GLDAS
476 and AWRA model data.

477 In Fig. 9, correlation between soil moisture products and precipitation (from ERA-
478 Interim) is shown, where the spatial variability of GLDAS (in A) seems to be smoother
479 compared to AWRA (in B). Figure 9 (B) indicates low correlation regions along the
480 Jason-2 pass of 064, 075, and 151 (Fig. 1 (A)) while these do not appear in the GLDAS
481 results (Fig. 9 (A)).

482 Both ARSSM sets (based on EOFs of GLDAS and AWRA) follow closely precipitation
483 (see Fig. 9 (C) and (D)). The magnitude of the correlations is found to be relatively higher
484 than for of models (compare Fig. 9 (A) and (B) to (C) and (D), see also the values in
485 Table 3).

486 The variability of soil moisture within the region A is examined by estimating standard
487 deviations at along-track altimetry positions (see also Table 4). Standard deviations
488 between $0.04 m^3/m^3$ and $0.06 m^3/m^3$ are found from the GLDAS simulations (Fig. 10
489 (A)), while the magnitude of AWRA simulations (Fig. 10 (B)) is larger than GLDAS
490 in the southwest. A region of very low standard deviations is found in the eastern part
491 along the tracks 038 and 151 (Fig. 1 (A)) that is located within the Gibson Desert
492 region (Fig. 10 (A)). In the northern and central parts of the study area A, we find
493 medium temporal variations which are slightly larger than those of GLDAS. The overall
494 variability of ARSSM sets depends on the models employed for estimating EOFs used in
495 the inversion (Fig. 10 (A) and (C), and Fig. 10 (B) and (D)). Considering the along-track
496 variabilities, it is clear that ARSSM sets represent higher spatial resolution than models
497 (compare along-track patterns of Fig. 10 (C) with (A), and Fig. 10 (D) with (B)).

498 In Fig. 11 (A), the magnitude of soil moisture from SMOS is shown which is generally
499 stronger compared to models and ARSSM (in Fig. 10). The SMOS results can indepen-
500 dently assess other soil moisture products. For instance, correlation coefficients between
501 ARSSM, employing the EOFs of AWRA, and SMOS are found to be relatively larger
502 (0.6 - 0.8) in many areas. With respect to the eastern part of the study region, along
503 the pass 151 we find low correlations over the Gibson Desert region due to the AWRA
504 base functions used here. Correlations between SMOS and ARSSM based on EOFs from
505 GLDAS in this region agree much better (not shown here). Lower correlation coefficients
506 in the northwestern part are related to the rapid changes in topography within this region
507 (Fig. 11 (B)).

508 5.3.2. Soil Moisture within Southwestern Australia (Study Region B)

509 ARSSM estimations (2002-2010), derived from the Ku-Band of Envisat within the
510 study region B (Fig. 1), are examined in this section. The groundtracks of Envisat are
511 denser than those of Jason-2 and they provide the chance to assess the quality of ARSSM
512 over different vegetation classes. In the light of previous results, since selecting EOFs
513 from AWRA or GLDAS does not significantly alter ARSSM estimations, we limit our
514 results to the ARSSM inverted by fitting the EOFs of the AWRA model.

Table 3: An overview over the median, minimum, and maximum correlation between Jason-2 ARSSM and model data from GLDAS, AWRA and ERA-Interim precipitation, as well as SMOS ascending and descending orbits is provided for study area A (Fig. 1, (A)). The individual rows are associated to ARSSM from using Ku- and C-Band, as well as EOFs from either GLDAS or AWRA model data. The number of points used for computation was 29271.

	GLDAS	AWRA	ERA-I	SMOS _{asc}	SMOS _{desc}
ARSSM ^{Ku} _{GLDAS}	0.60	0.49	0.55	0.68	0.63
[min max]	[0.19 0.83]	[-0.08 0.81]	[0.19 0.88]	[0.02 0.91]	[-0.23 0.92]
ARSSM ^C _{GLDAS}	0.60	0.48	0.55	0.70	0.65
[min max]	[0.17 0.84]	[-0.16 0.79]	[0.25 0.84]	[-0.05 0.93]	[-0.16 0.92]
ARSSM ^{Ku} _{AWRA}	0.58	0.48	0.55	0.67	0.61
[min max]	[-0.13 0.83]	[-0.21 0.77]	[-0.20 0.88]	[-0.32 0.90]	[-0.31 0.93]
ARSSM ^C _{AWRA}	0.57	0.46	0.52	0.68	0.63
[min max]	[-0.12 0.85]	[-0.32 0.80]	[-0.23 0.84]	[-0.27 0.93]	[-0.29 0.94]

Table 4: Overview over the median, minimum, and maximum standard deviations (SD) of SSM from ARSSM using Ku- and C-Band, as well as EOFs from AWRA and GLDAS for study area A (Fig. 1, (A)); furthermore, standard deviations from the GLDAS and AWRA model, as well as SMOS ascending and descending orbits are included. Standard deviations are provided in [m^3/m^3]. The number of points used for computation was 29271.

	SD_{median}	SD_{min}	SD_{max}
ARSSM ^{Ku} _{GLDAS}	0.045	0.021	0.068
ARSSM ^C _{GLDAS}	0.046	0.025	0.061
ARSSM ^{Ku} _{AWRA}	0.059	0	0.096
ARSSM ^C _{AWRA}	0.061	0	0.089
GLDAS	0.044	0.033	0.056
AWRA	0.058	0	0.098
SMOS _{asc}	0.061	0.027	0.136
SMOS _{desc}	0.051	0.022	0.010

515 Standard deviations of soil moisture products are shown in Fig. 12 (A), (B), and (C),
516 which indicate stronger variability compared to the region A. Similar signal strength is
517 found between ARSSM and AWRA simulations (~ 0.08 and $0.12 m^3/m^3$ in Fig. 12 (A)
518 and (B)) and relatively larger than that of GLDAS (~ 0.04 and $0.06 m^3/m^3$ in Fig. 12
519 (C)). This agrees with the results from before (Fig. 10). Considering the ARSSM results
520 in Fig. 12 (A), two small areas with relatively low standard deviations are identified: in
521 the north, where the pass 0950 and 0307 meet (see Fig. 1 (B)) the first area corresponds
522 to the altimeter crossing the Lakes Deborah and Seabrook and the second area in the

Table 5: Overview over the median, minimum, and maximum standard deviations (SD) of SSM from ARSSM using Ku-Band and EOFs from AWRA for study area B (Fig. 1, (B)); furthermore, standard deviations from the GLDAS and AWRA model are included. Standard deviations are provided in $[m^3/m^3]$. The number of points used for computation was 16350.

	SD_{median}	SD_{min}	SD_{max}
ARSSM ^{Ku} _{GLDAS}	0.089	0.024	0.163
GLDAS	0.050	0.037	0.070
AWRA	0.089	0.058	0.106

523 east, along the pass 0778 (see Fig. 1 (B)), is associated with the altimeter crossing Lake
 524 Cowan. The return signal from these large surface waters completely dominates the
 525 backscatter at these locations, which results in less meaningful ARSSM estimations.

526 Correlation between ARSSM and AWRA and GLDAS is shown in Fig. 12 (D) and
 527 (E), where we find values of more than 0.5 over the central and eastern parts of the region
 528 B with land cover classes ranging from dry savanna and shrublands in the eastern parts
 529 to large agricultural areas in the center. In the west and southwest, close to the coast, the
 530 correlation coefficients are relatively low < 0.2 , where the land is covered by dense forest.
 531 Additionally, close to Perth located at the west coast (Fig. 1 (B)), we find significantly
 532 lower correlations. It is interesting to note that the correlation coefficients of ARSSM
 533 with both AWRA and GLDAS are significantly higher in the descending altimetry tracks
 534 (even pass numbers in Fig. 1 (B)) than for the ascending tracks (odd pass numbers in
 535 Fig. 1 (B)).

536 ARSSM and 3-day accumulated precipitation data from ERA-Interim (Fig. 12 (F))
 537 are found to be virtually unrelated in the central and western, as well as in the south-
 538 eastern parts of the study region. Moderate correlation coefficients are found in the
 539 east and northeast parts of the region B. A similar pattern is observed when correlating
 540 soil moisture from AWRA simulated model data with 3-day accumulated ERA-Interim
 541 precipitation information (not shown here).

Table 6: An overview over the median, minimum, and maximum correlation between Envisat ARSSM and model data from GLDAS, AWRA and ERA-Interim precipitation is provided for study area B (Fig. 1, (B)). The number of points used for computation was 16350.

	GLDAS	AWRA	ERA-I
ARSSM ^{Ku} _{AWRA}	0.61	0.55	0.23
[min max]	[-0.09 0.83]	[-0.12 0.89]	[-0.22 0.67]

6. Discussion

6.1. Assessing the Level of Agreement between the ARSSM and Model Simulation/ SMOS

In this study, we first confirmed that there is a good correspondence between altimetry backscatter and available model derived soil moisture simulations within the (semi-)arid region of Western Australia (see Fig. 3). This relationship has already been investigated for other regions (Ridley et al., 1996; Papa et al., 2003; Fatras et al., 2012, 2015). We proceeded to apply altimetry backscatter for estimating surface soil moisture (SSM) information using a novel approach. Before, Fatras et al. (2012) assumed a direct linear relationship between backscatter and SSM. A similar approach was proposed by Wagner et al. (1999) for scatterometer data. In contrast, our approach relies on spatial information based on model data to constrain the altimetry derived backscatter and convert them to the SSM values.

The altimetry backscatter used in this study is a (slightly) modified version of the backscatter from the ICE-1 retracker (Martin et al., 1983), which allows us to suppress the effects of peaks, located on the trailing edge of the waveform, on the backscatter estimations. These peaks are often caused by open water located in the off-nadir direction. After applying the modification in equation (4), smoother backscatter values are derived compared to those from the ICE-1 method (see Fig. 2) especially close to surface waters. Fatras et al. (2012) investigated backscatter from different available retracking methods (while considering Envisat data over Sahel) and concluded that ICE-1 was best suited for deriving SSM. Generally we believe that developing a more specialized retracking method for retrieving land surface backscatter would improve the results.

We interpolated all available data sets spatially and temporally to the altimeter

565 ground track and times of crossing the study areas, respectively. This is an impor-
566 tant step since, e.g., simply using model data with a higher temporal resolution to derive
567 the EOFs would introduce artificial features, which may not be resolved by altimetry.
568 The spatial interpolation allows us to handle each altimeter track individually. Fatras
569 et al. (2015) averaged all altimetry data within a defined region in order to compare them
570 with other data with a different spatial resolution. However, we believe that the high
571 along-track resolution of altimetry is one of its greatest benefits and should be kept.

572 In the next step, the differences between successive cycles are computed to reduce
573 influences from surface features, such as topography, surface roughness and to some ex-
574 tent vegetation, which can be assumed either constant or varying slowly compared to the
575 repeat periods. As a result, we reconstruct anomalies of surface soil moisture rather than
576 absolute values. Other studies (Fatras et al., 2012, 2015) identified significant seasonal
577 cycles in the backscatter values over lands. For Western Australia, we found only a very
578 small annual amplitude in the ARSSM and simulated anomalies. The proposed approach
579 can also be applied to the absolute backscatter observations, without subtracting succes-
580 sive cycles. In this case, one has to remove the seasonal cycles before computing quality
581 measures such as correlation.

582 Direct comparisons between ARSSM, AWRA model data and SMOS (e.g. Fig. 5)
583 reveal that ARSSM corresponds well to SMOS derived SSM while not necessarily agreeing
584 with the model data although the same models data was used for implementing the
585 inversion. This indicates that our ARSSM is only constrained by the spatial information
586 extracted from the model data but the temporal evolutions carry the characteristics of
587 the backscatter measured by altimetry. The differences between model simulations and
588 ARSSM/SMOS might also be related to the temporal sampling. For example, AWRA
589 produces daily averages of top level soil moisture, which are not identical with altimetry
590 samples that are collected in a few minutes from Western Australia.

591 *6.2. Along-Track Behavior of the ARSSM*

592 Along-track correlations between AWRA model data with GLDAS model data, Ku-
593 and C-Band ARSSM, as well as SMOS data (from ascending and descending passes) are

594 investigated (Fig. 6). The results from Ku- and C-Band are closely related although
595 C-Band would theoretically be better suited to derive soil moisture information due to
596 its longer wavelength that allows better penetrating the canopy layers (Fatras et al.,
597 2015). Previous studies have also found little influence from vegetation on the mea-
598 sured nadir backscatter from altimetry (Fatras et al., 2012, 2015), within (semi-)arid
599 regions, which explains the similar performance of the Ku- and C-Band within Western
600 Australia. Higher correlations are found between the ascending SMOS data and AR-
601 SSM/model compared to descending orbits. This is likely related to the sampling time
602 i.e ~ 6 h local time at the equator for the ascending and ~ 18 h local time at the equator
603 for the descending orbits (Kerr et al., 2012). For Envisat Ku- and S-Band, Fatras et al.
604 (2012) suggested that computing differences between the two bands likely represent infor-
605 mation on soil moisture storage of different depth. However, we find a weak correlation
606 coefficients with AWRA, especially in the South (less than ~ 0.3 between $24^\circ S$ and $18^\circ S$),
607 and therefore we exclude its discussion in the rest of the study.

608 Since soil moisture in Australia is primarily driven by precipitation (Bartalis et al.,
609 2007; Draper et al., 2009), we also correlated soil moisture products to 3-day accumulated
610 precipitation anomalies derived from the ERA-Interim reanalysis product (see Fig. 7).
611 The 3-day period is selected following Ridley et al. (1996)'s recommendation that stated
612 in the Australian Simpson Desert the influence from precipitation on measured SSM
613 rapidly starts to fade after about two days. Larger correlation coefficients are found
614 between precipitation and ARSSM compared to model simulations. This indicates that
615 altimetry measurements are more sensitive to wet surface conditions, especially in the
616 first few centimeters of soil. For AWRA, we found weak correlations with precipitation
617 in the South in contrast to relatively higher and stable correlations between GLDAS
618 and precipitation. Weaker correlations of AWRA in the southern part of pass 075 seem
619 to be justified since precipitation is not the sole driver of soil moisture changes in that
620 region. We also find that the surface soil moisture barely increases in the Australian
621 desert regions even after heavy rainfall events, which is related to high evaporation rates
622 in this region (see also Ridley et al., 1996). This is also confirmed by expanding the
623 examination with respect to ARSSM and model data from GLDAS and AWRA to all

624 altimetry tracks in our study region A (Fig. 9).

625 Correlation coefficients between SMOS products and precipitation are found to be
626 similar to those of ARSSM and precipitation in the south (up to $25^{\circ}S$) indicating that
627 SMOS is also sensitive to wet surfaces. In the north, however, unlike all other products,
628 SMOS indicates smaller correlations with precipitation. More research is required to
629 address this inconsistency between SMOS and other soil moisture products.

630 *6.3. Surface Soil Moisture Anomalies within Western Australia*

631 ARSSM based on EOFs from, GLDAS and AWRA model data show better correlation
632 coefficients with GLDAS for all Jason-2 tracks inside study region A (Fig. 1, (A)). This is
633 likely related to the higher temporal resolution of GLDAS, which provides soil moisture
634 values every 3 hours (Rodell et al., 2004). Similarly, higher correlations are found between
635 SMOS and GLDAS compared to SMOS and AWRA.

636 Strong similarities between Fig. 8 (C) and (E), as well as between Fig. 8 (D) and
637 (F) indicate that introducing EOFs in the inversion acts as a constraint to reduce the
638 noisy behavior of backscatter, and the final ARSSM results do not significantly depend
639 on the chosen model base functions (from AWRA or GLDAS). However, since the spatial
640 resolution of GLDAS is low, one must carefully select the study regions sufficiently large
641 enough to have meaningful EOFs.

642 Over the Gibson Desert (Fig. 1, (A)), low correlations are found between ARSSM
643 and simulated soil moisture model data (Fig. 8), precipitation (Fig. 9), as well as SMOS
644 observations (Fig. 11, (B)). Low standard deviations are also detected in this region (Fig.
645 10). Soil moisture simulations from AWRA are not able to reflect the small changes and
646 thus the outputs include only zero values over this region during 2008-2011. As a result,
647 the EOFs derived from AWRA over this region are also zero, which consequently, limits
648 the estimation of ARSSM within this region.

649 Analyzing the standard deviations indicates that the amplitude of ARSSM (Fig. 10)
650 strongly depends on the standard deviations of a-priori models. For example lower stan-
651 dard deviations are expected from GLDAS since its spatial resolution is lower than
652 AWRA. Comparisons with SMOS (Fig. 11, (A)) indicate closer correspondence with

653 ARSSM inverted based on the AWRA's EOFs. These findings are also supported by
654 comparing the standard deviations in the study area B (Fig. 1, (B)) for ARSSM based
655 on Envisat backscatter and the two model data sets (Fig. 12, (A)-(C)).

656 The good correlation between ARSSM and SMOS, as an independent measurement
657 of SSM, indicates that the proposed approach to reconstruct SSM from altimetry works
658 well. Small discrepancies are found over regions in the North, which are co-located with
659 significant elevation anomalies. Rapid elevation changes will affect the retrieved signal on
660 the altimetry satellite since the range window on-board of the satellite is not able to adapt
661 to rapid changes in topography. This effect will be filtered in future implementations of
662 the algorithm.

663 In the study area B (Fig. 1, (B)), the Envisat Ku-Band data in combination with
664 EOFs derived from AWRA model data are used to derive ARSSM. The results are then
665 correlated with the simulations of AWRA and GLDAS (Fig. 11, (D) and (E)). The
666 ARSSM results are found to be sensitive to the land cover, whereas higher correlations
667 are found over shrublands, savanna and agricultural land compared to dense forests or
668 cities. In such regions, the altimetry signal cannot penetrate well through the trees or
669 buildings and, thus, contains little information about SSM. A similar observation can
670 be made for the correlations with precipitation over agricultural surfaces compared to
671 shrublands or savanna (Fig. 12, (F)). Over agricultural surfaces, the correlation is found
672 to be significantly smaller which is likely related to irrigation during periods of low
673 precipitation.

674 Higher correlations are found between ARSSM computed from ascending tracks and
675 models compared to the descending tracks. A possible explanation for this effect is the
676 time difference between altimetry measurements. Envisat flies on an almost perfect 35-
677 day repeat orbit. As a result, over region B, all ascending track measurements refer to
678 times between 2pm and 3pm UTC, while all descending measurements are between 1am
679 and 2am UTC. This means that the surface conditions observed by the altimeter are
680 quite different between the night- and day-time, and therefore this difference should be
681 considered for future applications and when comparing to different data sets. Another
682 aspect could be the influence of dew during night-time that has been suggested by Ridley

683 et al. (1996). This effect is reflected in the ARSSM but is not included in the soil moisture
684 model data simulations.

685 *6.4. Residuals of ARSSM and Model Simulations*

686 In Fig. 13, principal component analysis (PCA, equation (5)) is applied to the dif-
687 ferences of ARSSM and model simulations, from which only the first dominant mode is
688 shown. To compute the residuals with respect to the AWRA simulations (Fig. 13 (A)
689 and (B)), ARSSM are inverted using the EOFs of AWRA. Similarly, ARSSM in Fig.
690 13 (C) and (D) are inverted using the EOFs of GLDAS before computing the residuals
691 with GLDAS simulations. Therefore, the residuals are estimated in a consistent manner
692 and indicate the contribution of the new products in improving the estimation of spatio-
693 temporal variability of soil moisture within West Australia. The dominant temporal
694 patterns (Fig. 13 (B) and (D)) do not indicate seasonal differences between ARSSM and
695 model simulations but rather noise-like or related to individual events. The strong peaks
696 in the early 2009 and 2011 coincide with fairly strong precipitation events (precipitation
697 results are not shown). Strong differences with AWRA are found in the northeast of
698 region A, where AWRA is also not consistent with SMOS and GLDAS products. The
699 differences between ARSSM and GLDAS are distributed over the entire region A with
700 stronger anomalies over the southern parts. In the same region, we identify smaller
701 residuals between ARSSM and GLDAS model data. The reason for these differences
702 with GLDAS simulations is mainly related to the coarse resolution of its simulation com-
703 pared to the sampling of altimetry observations. Residuals between ARSSM and model
704 simulations have also been derived over the region B, but are not discussed here.

705 **7. Conclusion**

706 A novel approach is presented to invert satellite radar altimetry backscatter to surface
707 soil moisture. The conversion is performed via an inversion in which spatial empirical
708 orthogonal functions (EOFs) from model simulations are fitted to backscatter observa-
709 tions, and used to produce altimetry reconstructed surface soil moisture (ARSSM). These

710 new data have high along-track measurement rate, but the separation between individual
711 groundtracks is relatively large leading to a limited spatial coverage.

712 We have been able to confirm the correspondence between altimetry measured backscat-
713 ter and land surface features, such as surface roughness, topography, vegetation and,
714 especially, soil moisture. Validations of ARSSM against GLDAS and AWRA simulations
715 indicate higher correlation coefficients compared to directly using the backscatter obser-
716 vations. Along-track investigations also showed ARSSM to compare well to the SMOS
717 L3 products (maximum correlations of more than 0.8). Generally, the ARSSM are found
718 to be in better agreement with the GLDAS model data, independent of the model data
719 employed in the inversion. Stronger correlation coefficients are found between ARSSM
720 and precipitation data compared to those between model simulations and precipitation
721 indicating a higher sensitivity of ARSSM and SMOS to precipitation events. For future
722 work, it makes sense to compare the results to regional high resolution precipitation
723 products, such as those in Jeffrey et al. (2001) or Jones et al. (2009).

724 In the southern study region, generally, a strong agreement is found between ARSSM
725 and model simulations, where the value of correlation coefficients depends mostly on the
726 land cover below the altimetry track, i.e. showing smaller values over dense forest areas or
727 cities while stronger values are found over shrublands, savanna or agricultural land. Some
728 connections are also found with respect to the time of day, when the altimeter measures
729 backscatter signal. Envisat measurements along the ascending tracks are collected during
730 the night, while all the descending tracks refer to the measurements about 12 hours later
731 during the day. Weaker correlation coefficients are found between the latter and the daily
732 mean soil moisture simulated by the models.

733 We are confident that backscatter from altimetry can provide an independent addi-
734 tional data set of surface soil moisture to extend and support the information available
735 from existing soil moisture missions, such as SMOS or ASCAT. Starting in 1993, altime-
736 ters may be able to provide at least two decades of continuous time series of backscatter
737 measurements along the altimetry tracks. Combining altimetry with spatial information
738 derived from high resolution model data for a specific region allows to measure soil mois-
739 ture changes with high spatial resolution along the altimetry track. The Surface Water

740 and Ocean Topography (SWOT) mission will allow to not only cover the nadir regions,
741 but also two swaths of about 120km to each side of the ground track, which also shows
742 some potential for measuring soil moisture.

743 In this study, additional influences on the altimetry backscatter signal by vegeta-
744 tion have not been considered. Although, we expect these influences to be small after
745 computing temporal differences, and due to the nadir looking sensors of the altimeter
746 compared to the side looking radar systems, they might still be significant over strongly
747 vegetated regions, e.g., over the agricultural regions in southwestern Australia. Involving
748 these impacts within the proposed inversion will be considered in the future to further
749 improve the reconstruction. Furthermore, assimilating ARSSM into land surface models
750 should be studied in future research.

751 **Acknowledgments**

752 The authors are grateful to Dr. Luigi Renzullo (CSIRO) and Albert I.J.M van Dijk
753 (ANU) for providing the AWRA simulations and to ESA and AVISO for providing the
754 altimetry data. We are also grateful to NASA and NOAA for providing the GLDAS
755 model simulations. The L3 SMOS data were produced by the Barcelona Expert Centre,
756 a joint initiative of the Spanish Research Council (CSIC) and Technical University of
757 Catalonia (UPC). We would also like to thank 3 anonymous reviewers and the associate
758 editor Tim McVicar for their detailed reviews, which greatly improved the quality of the
759 manuscript.

760 **References**

- 761 Al-Yaari, A., Wigneron, J., Ducharne, A., Kerr, Y., de Jeu, R., Schalie, R., Rodriguez-
762 Fernandez, N., Drusch, M., Dolman, H., & Mecklenburg, S. (2015). Testing simple
763 regression equations to derive long-term global soil moisture datasets from satellite-
764 based brightness temperature observations. In *2. SMOS Science Conference, Madrid, ESP (2015-05-25 - 2015-05-29)*. URL: <http://prodinra.inra.fr/record/305851>.
765
- 766 Angiuli, E., del Frate, F., & Monerris, A. (2008). Application of neural networks to
767 soil moisture retrievals from l-band radiometric data. In *IGARSS 2008 - 2008 IEEE*
768 *International Geoscience and Remote Sensing Symposium*. volume 2. doi:10.1109/
769 IGARSS.2008.4778927.
- 770 AVISO (2015). *OSTM / Jason-2 Products Handbook*. CNES / NASA <http://www.>
771 [aviso.altimetry.fr](http://www.aviso.altimetry.fr). SALP-MU-M-OP-15815-CN, Issue 1.9.
- 772 Bartalis, Z., Wagner, W., Naeimi, V., Hasenauer, S., Scipal, K., Bonekamp, H., Figa,
773 J., & Anderson, C. (2007). Initial soil moisture retrieval from the metop-a advanced
774 scatterometer (ascat). *Geophysical Research Letters*, *34*. doi:10.1029/2007GL031088.
775 L20401.
- 776 Birkett, C. M., & Beckley, B. (2010). Investigating the performance of the Jason-2/OSTM
777 radar altimeter over lakes and reservoirs. *Marine Geodesy*, *33*, 204–238.
- 778 Blarel, F., Frappart, F., Legrésy, B., Blumstein, D., & Rémy, F. (2015). Altimetry
779 backscattering signatures at Ku and S bands over land ice and ice sheets. In *Proc.*
780 *SPIE 9637, Remote Sensing for Agriculture, Ecosystems, and Hydrology XVII, 963727*
781 *(October 14, 2015)*. doi:10.1117/12.2194498.
- 782 Brown, G. S. (1977). The average impulse response of a rough surface and its applications.
783 *IEEE Transactions on Antennas and Propagation*, *AP-25*, 67–74.
- 784 Chai, S.-S., Walker, J. P., Makarynskyy, O., Kuhn, M., Veenendaal, B., & West, G.
785 (2010). Use of Soil Moisture Variability in Artificial Neural Network Retrieval of Soil
786 Moisture. *Remote Sens.*, *2*, 166–190. doi:doi:10.3390/rs2010166.

- 787 Chelton, D. B., Ries, J. C., Haines, B. J., Fu, L.-L., & Callahan, P. S. (2001). Satellite
788 altimetry and earth sciences: A handbook of techniques and applications. chapter 1.
789 (pp. 1–132).
- 790 Dee, D. P., Uppala, S. M., Simmons, A. J., Berrisford, P., Poli, P., Kobayashi, S.,
791 Andrae, U., Balmaseda, M. A., Balsamo, G., Bauer, P., Bechtold, P., Beljaars, A.
792 C. M., van de Berg, L., Bidlot, J., Bormann, N., Delsol, C., Dragani, R., Fuentes,
793 M., Geer, A. J., Haimberger, L., Healy, S. B., Hersbach, H., Hólm, E. V., Isaksen,
794 L., Kállberg, P., Köhler, M., Matricardi, M., McNally, A. P., Monge-Sanz, B. M.,
795 Morcrette, J.-J., Park, B.-K., Peubey, C., de Rosnay, P., Tavolato, C., Thépaut, J.-N.,
796 & Vitart, F. (2011). The era-interim reanalysis: configuration and performance of the
797 data assimilation system. *Quarterly Journal of the Royal Meteorological Society*, *137*,
798 553–597. doi:<http://dx.doi.org/10.1002/qj.828>.
- 799 Delwart, S., Bouzinac, C., Wursteisen, P., Berger, M., Drinkwater, M., Martin-Neira, M.,
800 & Kerr, Y. H. (2008). Smos validation and the cosmos campaigns. *IEEE Transactions*
801 *on Geoscience and Remote Sensing*, *46*, 695 – 704.
- 802 Deng, X., Featherstone, W. E., Hwang, C., & Berry, P. A. M. (2002). Estimation of
803 contamination of ers-2 and poseidon satellite radar altimetry close to the coasts of
804 australia. *Marine Geodesy*, *Vol. 25*, pp. 259–271. doi:10.108/01490410214990.
- 805 Desjonquères, J.-D., Carayon, G., Steunou, N., & Lambin, J. (2010). Poseidon-3 Radar
806 Altimeter: New Modes and In-Flight Performances. *Marine Geodesy*, *33(S1)*, 53–79.
807 doi:10.1080/01490419.2010.488970.
- 808 Donohue, R. J., McVicar, T. R., & Roderick, M. L. (2008). Climate-related trends in
809 Australian vegetation cover as inferred from satellite observations, 19812006. *Global*
810 *Change Biology*, *15*, 1025–1039. URL: [http://dx.doi.org/10.1111/j.1365-2486.](http://dx.doi.org/10.1111/j.1365-2486.2008.01746.x)
811 [2008.01746.x](http://dx.doi.org/10.1111/j.1365-2486.2008.01746.x). doi:10.1111/j.1365-2486.2008.01746.x.
- 812 Draper, C. S., Walker, J. P., Steinle, P. J., de Jeu, R. A. M., & Holmes, T. R. H.
813 (2009). An evaluation of amsre derived soil moisture over australia. *Remote Sensing*
814 *of Environment*, *113 (4)*, 703–710. doi:[doi:10.1016/j.rse.2008.11.011](http://dx.doi.org/10.1016/j.rse.2008.11.011).

815 Entekhabi, D., Njoku, E. G., O'Neill, P. E., Kellogg, K. H., Crow, W. T., Edelstein,
816 W. N., Entin, J. K., Goodman, S. D., Jackson, T. J., Johnson, J., Kimball, J., Piep-
817 meier, J. R., Koster, R. D., Martin, N., McDonald, K. C., Moghaddam, M., Moran,
818 S., Reichle, R., Shi, J. C., Spencer, M. W., Thurman, S. W., Tsang, L., & Zyl, J. V.
819 (2010). The soil moisture active passive (smap) mission. *Proceedings of the IEEE*, *98*,
820 704–716. doi:10.1109/JPROC.2010.2043918.

821 ESA (2007). *Envisat RA2/MWR Product Handbook*. European Space Agency (ESA)
822 <https://earth.esa.int/handbooks/ra2-mwr/>. URL: [https://earth.esa.int/](https://earth.esa.int/handbooks/ra2-mwr)
823 [handbooks/ra2-mwr](https://earth.esa.int/handbooks/ra2-mwr) issue 2.2.

824 ESA (2014). *SMOS Level 2 and Auxiliary Data Products Specifications*. European Space
825 Agency (ESA) [https://earth.esa.int/documents/10174/1854583/SMOS_L2_Aux_](https://earth.esa.int/documents/10174/1854583/SMOS_L2_Aux_Data_Product_Specification)
826 [Data_Product_Specification](https://earth.esa.int/documents/10174/1854583/SMOS_L2_Aux_Data_Product_Specification). URL: [https://earth.esa.int/documents/10174/](https://earth.esa.int/documents/10174/1854583/SMOS_L2_Aux_Data_Product_Specification)
827 [1854583/SMOS_L2_Aux_Data_Product_Specification](https://earth.esa.int/documents/10174/1854583/SMOS_L2_Aux_Data_Product_Specification) issue 8/1.

828 Fatras, C., Frappart, F., Mougin, E., Frison, P.-L., Faye, G., P., B., & Jarlan, L. (2015).
829 Spaceborne altimetry and scatterometry backscattering signatures at C- and Ku-bands
830 over West Africa. *Remote Sensing of Environment*, *159*, 117–133. doi:10.1016/j.rse.
831 2014.12.005.

832 Fatras, C., Frappart, F., Mougin, E., Grippa, M., & Hiernaux, P. (2012). Estimating
833 surface soil moisture over sahel using envisat radar altimetry. *Remote Sensing of the*
834 *Environment*, *123*, 496 – 507.

835 Frappart, F., Fatras, C., Mougin, E., Marieu, V., Diepkilé, A. T., Blarel, F., & P., B.
836 (2015). Radar altimetry backscattering signatures at Ka, Ku, C and S bands over
837 West Africa. *Physics and Chemistry of the Earth*, *83-84*, 96–110. doi:10.1016/j.pce.
838 2015.05.001.

839 Glenn, E. P., Doody, T. M., Guerschman, J. P., Huete, A. R., King, E. A., McVicar,
840 T. R., Van Dijk, A. I. J. M., Van Niel, T. G., Yebra, M., & Zhang, Y. (2011). Actual
841 evapotranspiration estimation by ground and remote sensing methods: the australian

- 842 experience. *Hydrological Processes*, 25, 4103–4116. URL: <http://dx.doi.org/10.1002/hyp.8391>. doi:10.1002/hyp.8391.
- 843
- 844 Jeffrey, S. J., Carter, J. O., Moodie, K. B., & Beswick, A. R. (2001). Using spatial
845 interpolation to construct a comprehensive archive of Australian climate data. *Environ.
846 Model Software*, 16, 309 – 330. doi:10.1016/S1364-8152(01)00008-1.
- 847 Jones, D. A., Wang, W., & Fawcett, R. (2009). High-quality spatial climate data sets for
848 Australia. *Aust. Meteorol. Oceanogr.*, 58, 233 – 248.
- 849 Katul, G. G., Oren, R., Manzoni, S., Higgins, C., & Parlange, M. B. (2012). Evap-
850 otranspiration: a process driving mass transport and energy exchange in the soil-
851 plant-atmosphere-climate system. *Reviews of Geophysics*, 50, RG3002. doi:10.1029/
852 2011RG000366.
- 853 Kerr, Y. H., Waldteufel, P., Richaume, P., Wigneron, J. P., Ferrazzoli, P., Mahmoodi,
854 A., Al Bitar, A., Cabot, F., Gruhier, C., Juglea, S. E., Leroux, D., Mialon, A., &
855 Delwart, S. (2012). The smos soil moisture retrieval algorithm. *IEEE Transactions on
856 Geoscience and Remote Sensing*, 50, 1384–1403. doi:10.1109/TGRS.2012.2184548.
- 857 Liou, Y.-A., Liu, S.-F., & Wang, W.-J. (2001). Retrieving soil moisture from simulated
858 brightness temperatures by a neural network. *IEEE Transactions on Geoscience and
859 Remote Sensing*, 39, 1662–1672. doi:10.1109/36.942544.
- 860 Liu, Y. Y., Parinussa, R. M., Dorigo, W. A., De Jeu, R. A. M., Wagner, W., van Dijk, A.
861 I. J. M., McCabe, M. F., & Evans, J. P. (2011). Developing an improved soil moisture
862 dataset by blending passive and active microwave satellite-based retrievals. *Hydrology
863 and Earth System Sciences*, 15 (2), 425 – 436. doi:10.5194/hess-15-425-2011.
- 864 Martin, T. V., Zwally, H. J., Brenner, A. C., & Bindshadler, R. A. (1983). Analysis and
865 retracking of continental ice sheet radar altimeter waveforms. *J. Geophys. Res.*, 88,
866 1608–1616.
- 867 Montzka, C., Bogen, H., Weihermüller, L., Jonard, F., Bouzinac, C., Kainulainen, J.,
868 Balling, J. E., Loew, A., dall’Amico, J., Rouhe, E., Vanderborght, J., & Vereecken,

869 H. (2013). Brightness Temperature and Soil Moisture Validation at Different Scales
870 During the SMOS Validation Campaign in the Rur and Erft CCatchment, Germany.
871 *IEEE Transactions on Geoscience and Remote Sensing*, 51, 1728 – 1743. doi:10.1109/
872 TGRS.2012.2206031.

873 Mougin, E., Lopes, A., Frison, P.-L., & Proisy, C. (1995). Preliminary analysis of ERS-1
874 wind scatterometer data over land surfaces. *Int. J. Remote Sens.*, 6, 391 – 398.

875 Njoku, E. G., Jackson, T. J., Lakshmi, V., Chan, T. K., & Nghiem, S. V. (2003). Soil
876 moisture retrieval from amsr-e. *IEEE Transactions on Geoscience and Remote Sensing*,
877 41, 215 – 229. doi:10.1109/TGRS.2002.808243.

878 Papa, F., Legresy, B., & Remy, F. (2003). Use of the TopexPoseidon dual-frequency
879 radar altimeter over land surfaces. *Remote Sensing of Environment*, 87, 136 – 147.
880 doi:10.1016/S0034-4257(03)00136-6.

881 Piles, M., Camps, A., Vall-llossera, M., Corbella, I., Panciera, R., Rudiger, C., Kerr,
882 Y. H., & Walker, J. (2011). Downscaling SMOS-Derived Soil Moisture Using MODIS
883 Visible/Infrared Data. *IEEE Transactions on Geoscience and Remote Sensing*, 49,
884 3156–3166. doi:10.1109/TGRS.2011.2120615.

885 Preisendorfer, R. (1988). *Principal component analysis in meteorology and oceanography*.
886 Elsevier: Amsterdam.

887 Ridley, J., Strawbridge, F., Card, R., & Phillips, H. (1996). Radar Backscatter Charac-
888 teristics of a Desert Surface. *Remote Sensing of Environment*, 57(2), 63–78.

889 Roca, M., Jackson, H., & Celani, C. (2002). RA-2 Sigma-0 Absolute Calibration. In *Proc.*
890 *of Envisat Validation Workshop, Italy, 9 - 13 December 2002 (ESA SP-531, August*
891 *2003)*.

892 Rodell, M., Houser, P., Jambor, U., Gottschalck, J., Mitchell, K., Meng, C.-J., Arsenault,
893 K., Cosgrove, B., Radakovich, J., Bosilovich, M., Entin, J., Walker, J., Lohmann, D.,
894 & Toll, D. (2004). The global land data assimilation system. *Bulletin of the American*
895 *Meteorological Society*, 85(3), 381 – 394.

- 896 Rodríguez-Fernández, N. J., Aires, F., Richaume, P., Kerr, Y. H., Prigent, C., Kolassa,
897 J., Cabot, F., Jimnez, C., Mahmoodi, A., & Drusch, M. (2015). Soil Moisture Retrieval
898 Using Neural Networks: Application to SMOS. *IEEE Transactions on Geoscience and*
899 *Remote Sensing*, *53*, 5991–6007. doi:10.1109/TGRS.2015.2430845.
- 900 Rötzer, K., Montzka, C., Bogen, H., Wagner, W., Kerr, Y. H., Kidd, R., & Vereecken,
901 H. (2014). Catchment scale validation of SMOS and ASCAT soil moisture products
902 using hydrological modeling and temporal stability analysis. *Journal of Hydrology*,
903 *519*, 934 – 946. doi:10.1016/j.jhydrol.2014.07.065.
- 904 van der Schalie, R., Parinussa, R. M., Renzullo, L. J., van Dijk, A. I. J. M., Su, C.-H.,
905 & de Jeu, R. A. M. (2015). SMOS soil moisture retrievals using the land parameter
906 retrieval model: Evaluation over the Murrumbidgee Catchment, southeast Australia.
907 *Remote*, *163*, 70 – 79. doi:10.1016/j.rse.2015.03.006.
- 908 Shum, C. K., Ries, J. C., & Tapley, B. D. (1995). The accuracy and applications of
909 satellite altimetry. *Geophysical Journal International*, *121* (2), 321–336. doi:10.1111/
910 j.1365-246X.1995.tb05714.x.
- 911 SMOS-BEC (2015). *SMOS-BEC Ocean and Land Products Description*. Technical Re-
912 port Barcelona Expert Centre, Institute of Marine Sciences, CSIC. Barcelona, Spain.
913 Available at: <http://cp34-bec.cmima.csic.es/doc/BEC-SMOS-0001-PD.pdf>.
- 914 Ulaby, F., Moore, R., & Fung, A. (1982). Microwave remote sensing: Active and passive.
915 *Radar Remote Sensing and Surface Scattering and Emission*, *2*.
- 916 Vaze, J., Viney, N., Stenson, M., Renzullo, L., van Dijk, A., Dutta, D., Crosbie, R., Lerat,
917 J., Penton, D., Vleeshouwer, J., Peeters, L., Teng, J., Kim, S., Hughes, J., Dawes, W.,
918 Zhang, Y., Leighton, B., Perraud, J., Joehnk, K., Yang, A., Wang, B., Frost, A.,
919 Elmahdi, A., Smith, A., & Daamen, C. (2013). The Australian water resource assess-
920 ment modelling system (AWRA). *20th International Congress on Modelling and Sim-*
921 *ulation, Adelaide, Australia, 1-6 December 2013, www.mssanz.org.au/modsim2013, .*

922 Wagner, W., Lemoine, G., & Rott, H. (1999). A Method for Estimating Soil Moisture
923 from ERS Scatterometer and Soil Data. *Remote Sensing of Environment*, 70(2), 191
924 – 207. doi:10.1016/S0034-4257(99)00036-X.

925 Zelli, C. (1999). ENVISAT RA-2 advanced radar altimeter: Instrument design and pre-
926 launch performance assessment review. *Acta Astronaut.*, 44(7), 323–333.

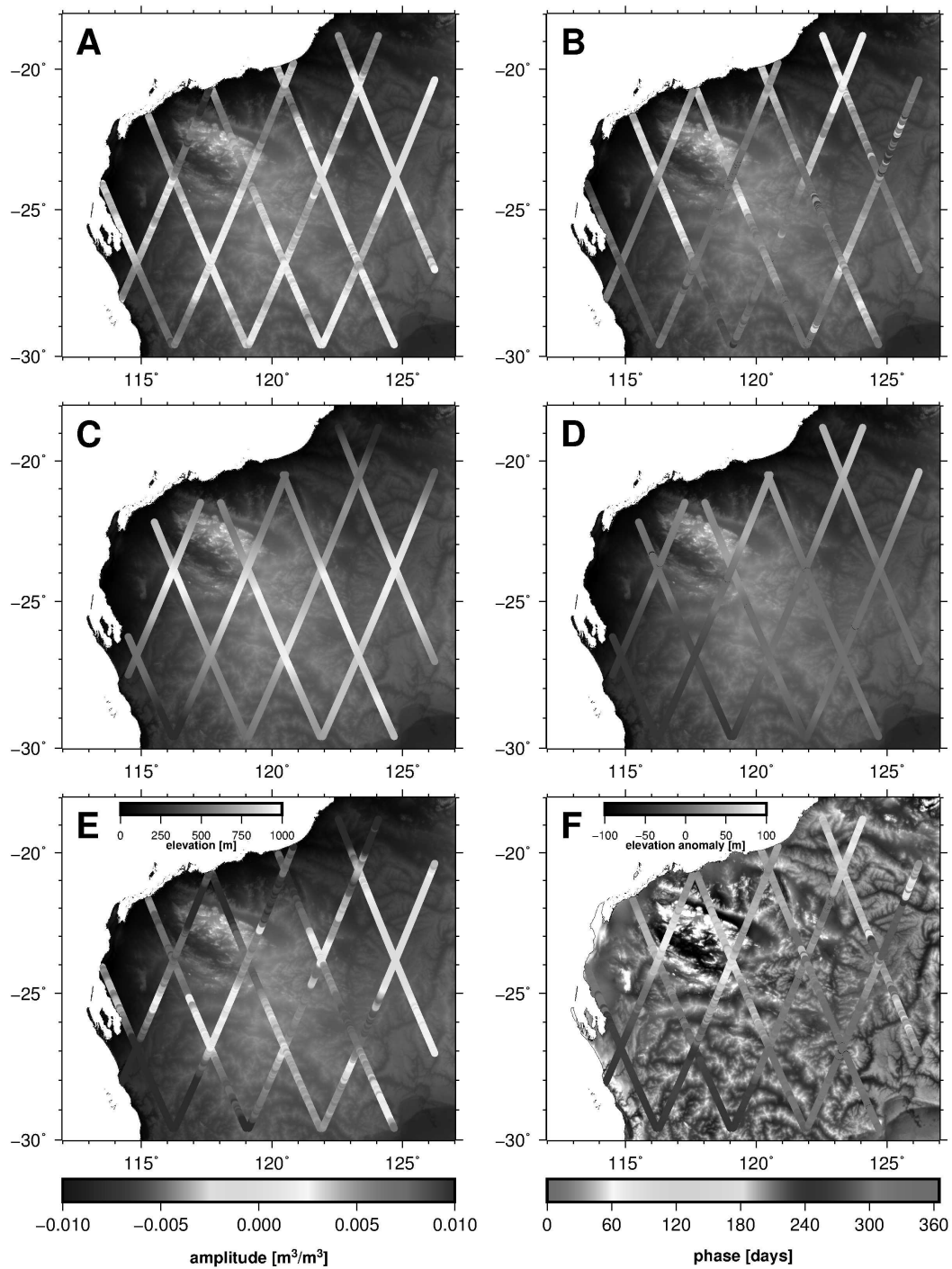


Figure 4: Comparison of annual amplitude and phase from Jason-2 C-Band ARSSM (A) and (B), using spatial base functions derived from the ARWA model, the GLDAS model (C) and (D), as well as the AWRA model (E) and (F).

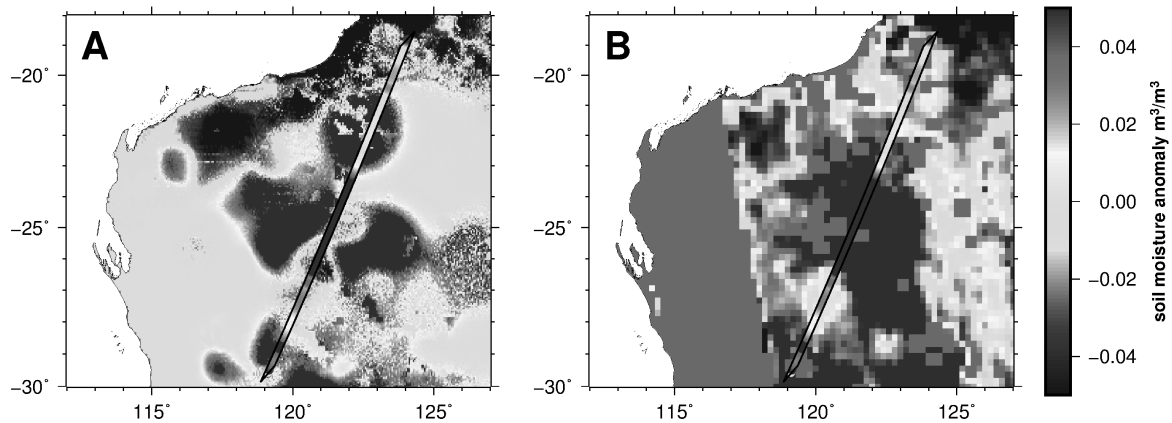


Figure 5: Comparison of soil moisture anomalies from Jason-2, pass 075, cycle 58 (January 31, 2010) with anomalies from (A) AWRA simulation and (B) SMOS products. Colors inside the black polygons represent ARSSM derived from Jason-2 C-Band.

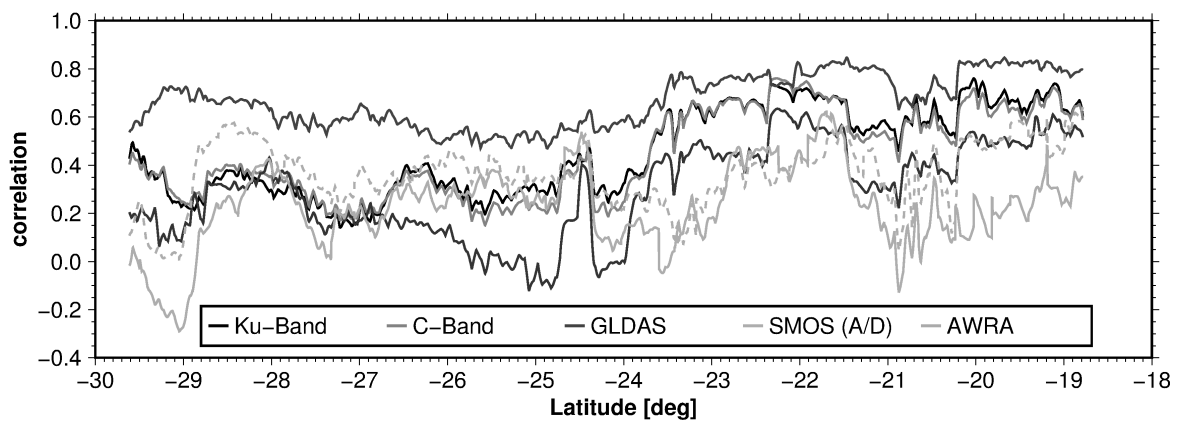


Figure 6: Correlation coefficients between the top level soil moisture anomalies derived from AWRA simulations and those of GLDAS, ARSSM, and SMOS measurements. The results are computed along the pass 075 of Jason-2 for the time period 2008-2011, where AWRA data was available. To estimate ARSSM, the EOFs of AWRA are used in the inversion to convert Ku- and C-Band backscatter measurements to soil moisture anomalies. For SMOS, the solid line refers to the correlation coefficients between descending orbit products and AWRA, while the dashed line corresponds to the ascending orbit products.

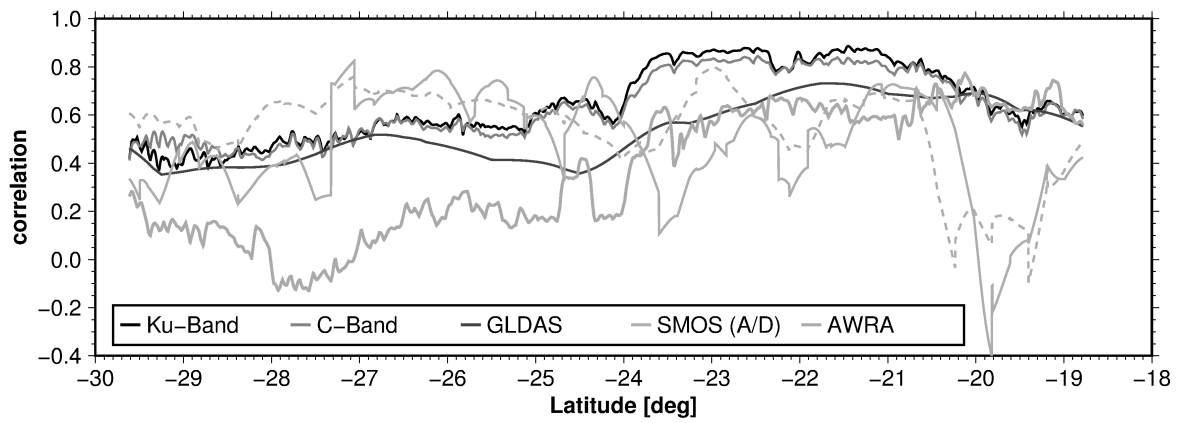


Figure 7: Correlation coefficients (2008-2010) between 3-day accumulated precipitation anomalies from ERA-Interim with ARSSM derived from the Ku- and C-Band of Jason-2 observations, as well as between precipitation anomalies and top level soil moisture information extracted from the GLDAS and AWRA model, and soil moisture derived from SMOS products. For the SMOS data, the solid line refers to the descending orbit, while the dashed line corresponds to the ascending orbit.

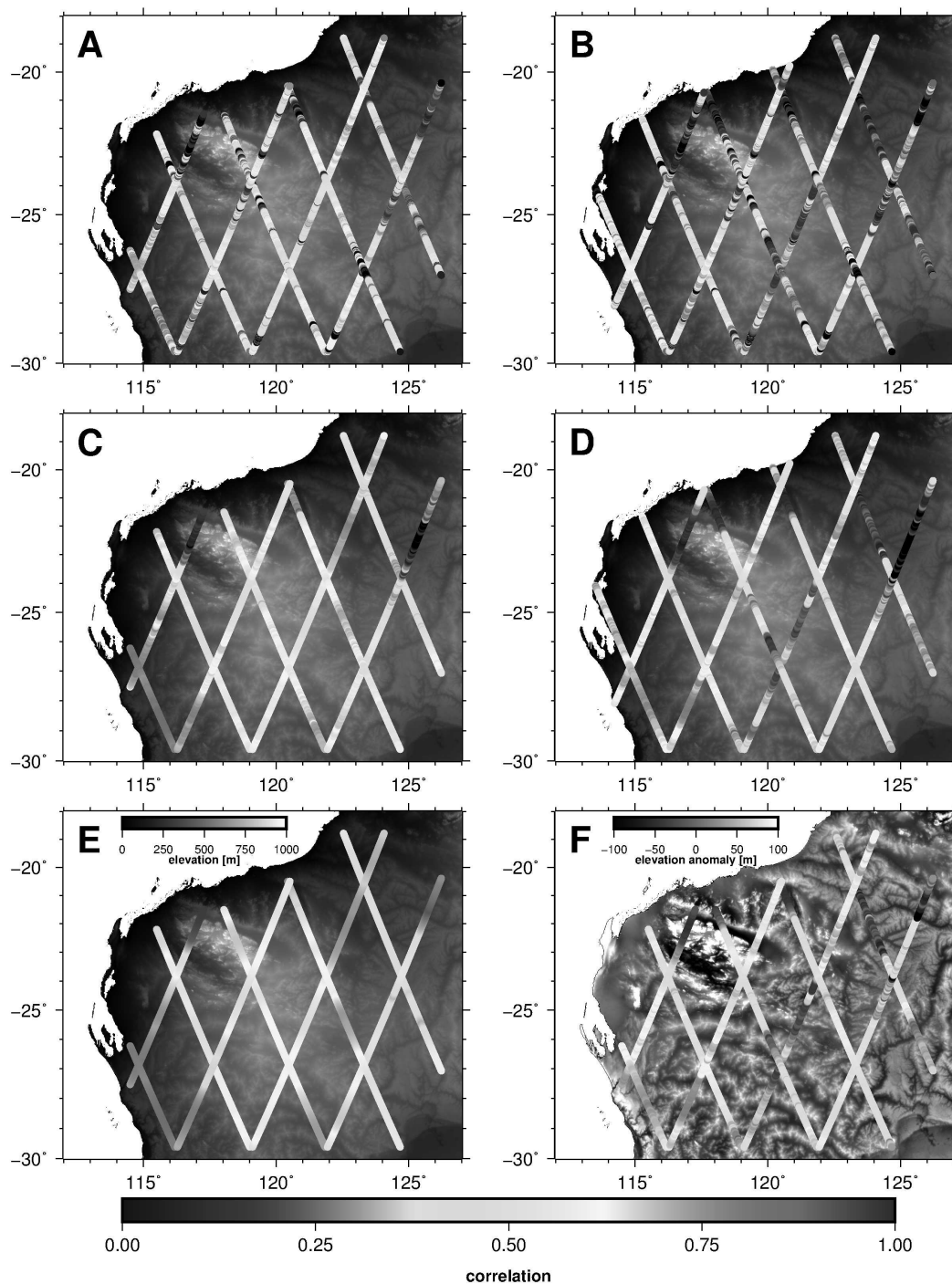


Figure 8: Comparisons between altimetry and model simulations. The first row shows correlations between C-Band backscatter with (A) GLDAS and (B) AWRA model simulations. In the second row, correlations between ARSSM from Jason-2 C-Band using EOFs based on AWRA model data and model data from (C) GLDAS and (D) AWRA are presented. The bottom row, shows correlations between ARSSM derived utilizing GLDAS EOFs and soil moisture model data from (E) GLDAS and (F) AWRA.

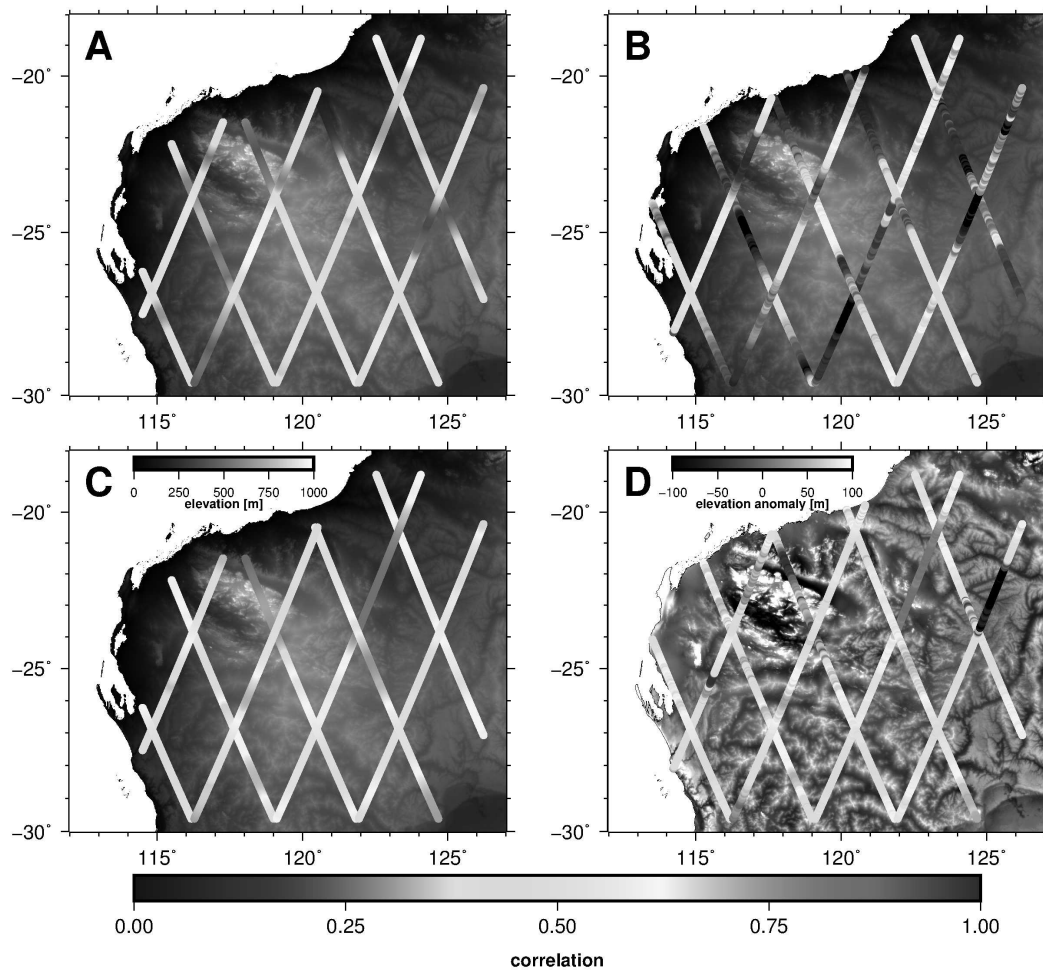


Figure 9: Correlations of ERA-Interim precipitation data with top level soil moisture model data from (A) GLDAS and (B) AWRA. Additionally, correlations between precipitation and ARSSM estimated based on spatial patterns from (C) GLDAS and (D) AWRA are shown.

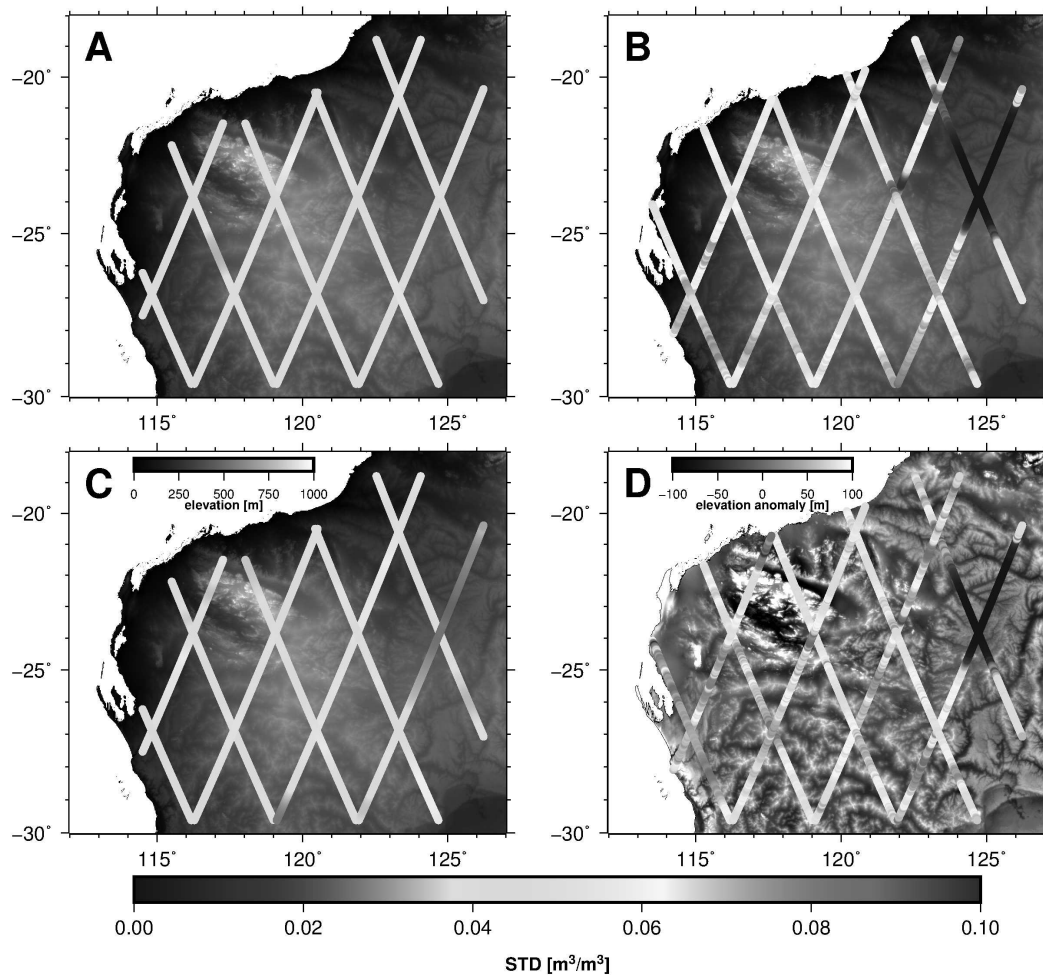


Figure 10: Standard deviations of (A) GLDAS model, (B) AWRA model data, (C) ARSSM based on GLDAS spatial patterns and (D) ARSSM estimated using spatial patterns derived from AWRA.

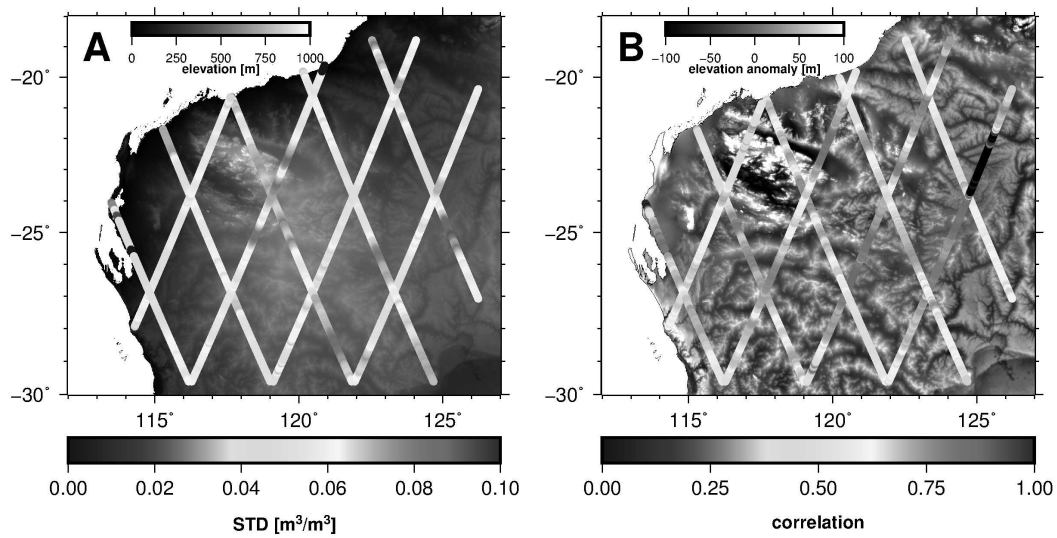


Figure 11: (A) Standard deviations of soil moisture anomalies based on SMOS product. (B) Correlation coefficients between SMOS soil moisture anomalies and ARSSM sets based on the C-Band observations and EOFs of AWRA.

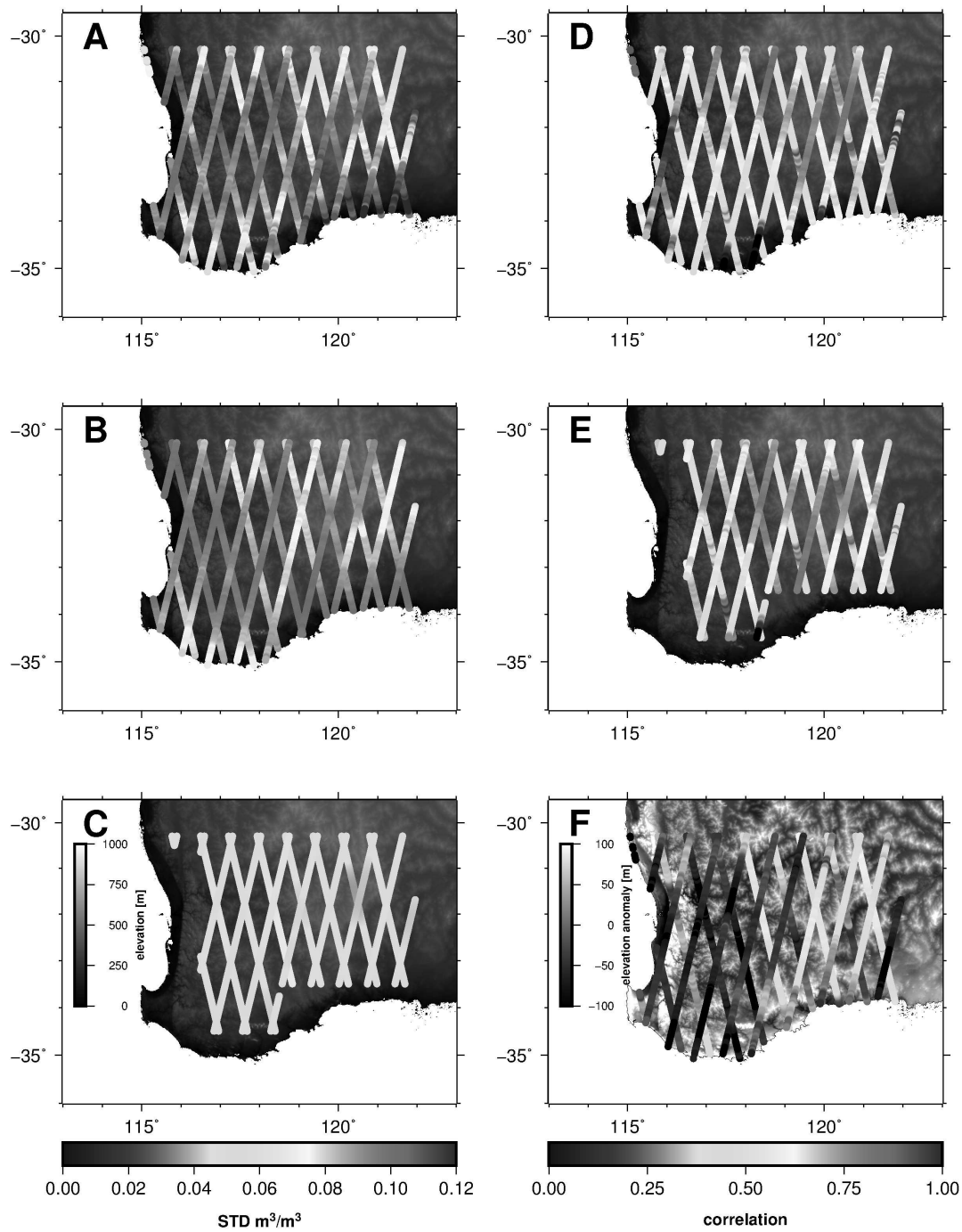


Figure 12: Soil moisture structure during 2002-2010. The first column shows the standard deviations of (A) ARSSM from the Ku-Band of Envisat, (B) AWRA simulations, and (C) GLDAS simulations. The second column includes the correlation coefficients between ARSSM in (A) with (D) AWRA simulations, (E) GLDAS simulations, and finally (E) ERA-Interim precipitation time series.

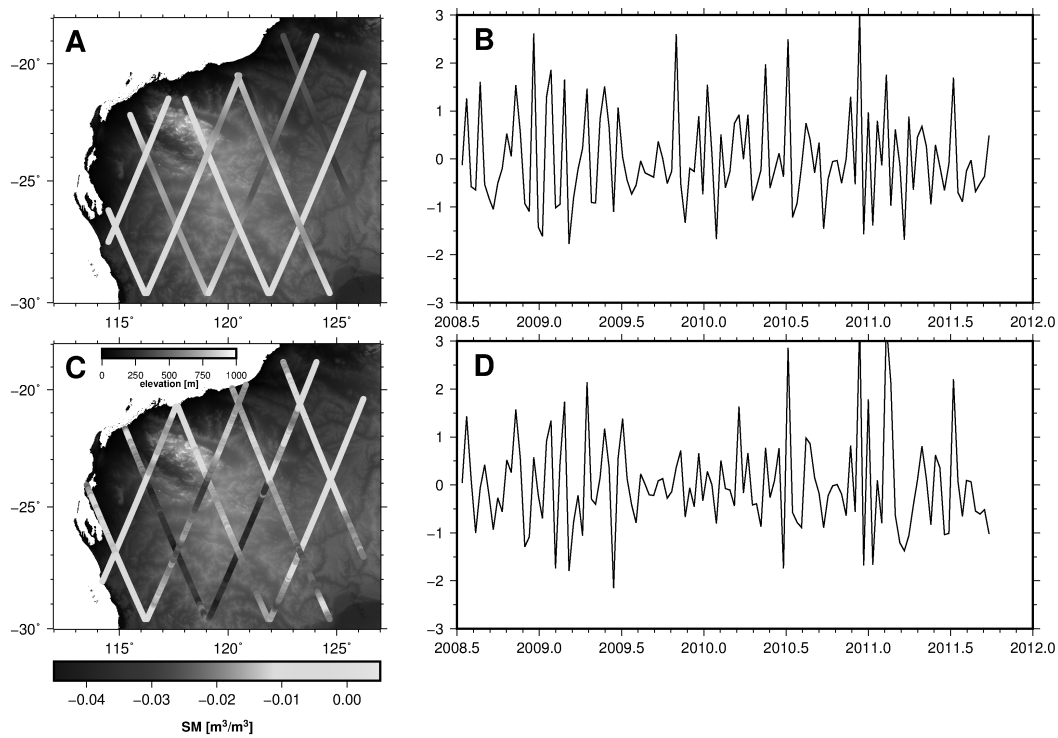


Figure 13: (A) First empirical orthogonal function (EOF) and (B) first principal component (PC) derived by applying SVD on the residuals of ARSSM and GLDAS (explaining 25.0% of the total variance of residuals). (C) First EOF and (D) first PC of the residuals of ARSSM and AWRA (explaining 20.1% of the total variance of residuals).